Heavy-ion collisions at the LHC

G. Roland,[1] K. Šafařík,[2] P. Steinberg,[3]

[1]MIT, USA
[2]CERN, Geneva, Switzerland
[3]Brookhaven National Laboratory, Brookhaven, NY, USA

December 10, 2013

Abstract

1 Introduction

1.1 Physics motivation

1.2 LHC heavy-ion running

Heavy ion running at the Large Hadron Collider had been planned long before the machine was built. This was based on the interest in the physics at the CERN SPS, which was colliding light ions since 1986 and heavy ions since 1994, and as a natural extension to the already-planned program at the Relativistic Heavy Ion Collider (RHIC). The accelerator complex is shown in Figure 1. Ions start their path to collisions at the ECR (electron cyclotron resonance) ion source, which provides lead ions stripped to values around Pb^{29+}, which are passed through a spectrometer to select Pb^{29+} and accelerated in a linear accelerator to 4.2 MeV/n. They are then stripped to around Pb^{54+} by a 0.3 μm carbon foil and the Pb^{54+} are selected by a spectrometer to be fed into the CERN Low Energy Ion Ring (LEIR). LEIR is used to transform a set of low intensity ion pulses from the LINAC into shorter bunches with higher intensity. This is done by filling the available phase space in three dimensions. After this, electron cooling is applied to shrink the beam to increase the bunch density, and decelerate it into "a stack sitting slightly inside the central orbit". At this point, seven pulses are captured, split into two bunches, and then accelerated to 72 MeV/n. The bunches from LEIR are then sent to the CERN PS (Proton Synchrotron), accelerated to 5.9 GeV/n and stripped fully to Pb^{82+} using a 0.8 mm aluminium foil. These ions are then sent to the SPS where they are acceleated to 177 GeV/n and injected into the LHC.

To date, there have been three heavy ion runs at the LHC. The first run was in November/December 2010, which provided 120 colliding bunches of lead ions in each ring, with a center of mass energy per nucleon pair of $\sqrt{s_{NN}} = 2.76$ TeV, a peak luminosity of $3 \times 10^{25}/\text{cm}^2 s$ and an integrated luminosity of 7 μb^{-1}, corresponding to about 50 million minimum bias events. The second run was in November/December 2011, which provided about 360 colliding bunches of lead ions per ring, also at $\sqrt{s_{NN}} = 2.76$ TeV, a peak luminosity of about $5 \times 10^{26}/\text{cm}^2 s$ and an integrated luminosity of about 150
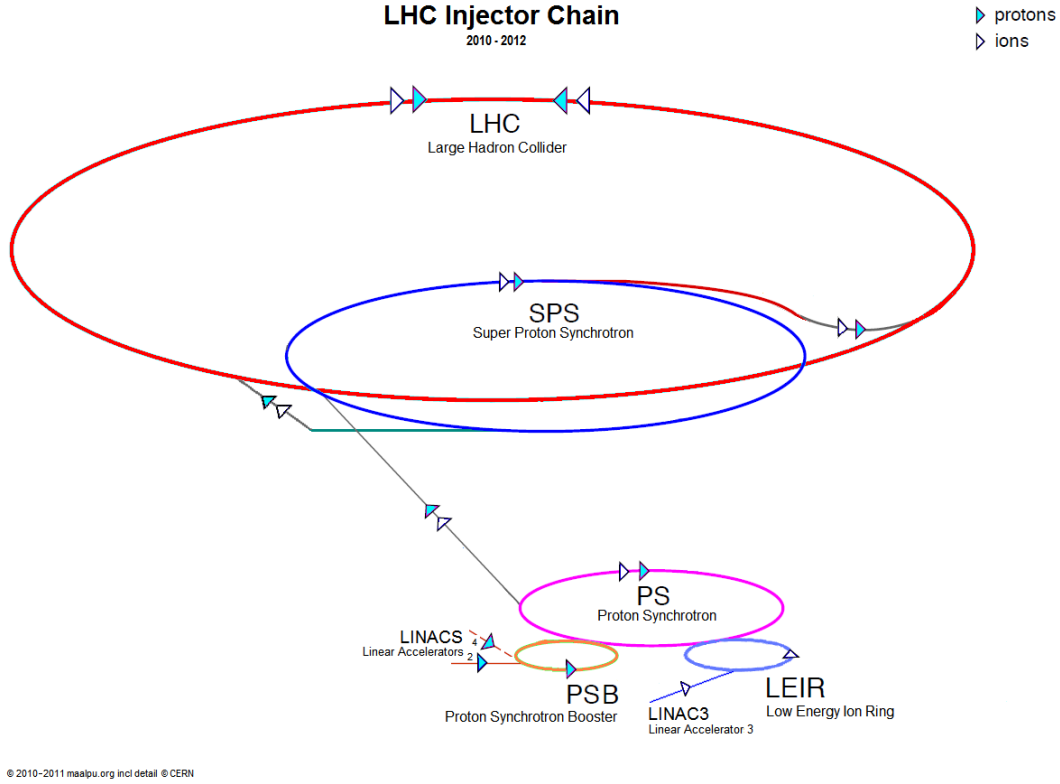
Figure 1: Schematic view of LHC injector chain, showing the path of both protons and ions.

μb^{-1}, a factor of 20 increase over 2010. The third run, in January/February 2013, provided proton-lead collisions at $\sqrt{s_{\mathrm{NN}}} = 5.02$ TeV but these results are not discussed in detail in this review.

1.3 Detectors at the LHC

1.3.1 ATLAS

The ATLAS detector, shown in Figure 2 is one of the general-purpose particle physics detectors at the LHC. It has three main detector systems: the inner detector (ID), the calorimeter, and the muon spectrometer (MS). The inner detector tracks charged particles using three separate detector technologies, and the spectrometer is immersed in a 2T axial field from a superconducting solenoid magnet 1.2m from the nominal beam axis. The pixel detector typically provides three high-resolution space points with three layers of pixel detector surrounding the beam pipe within $|z| < 400mm$ (covering approximately $|\eta| < 2$ and 4 disks at forward angles covering out to $|\eta| < 2.5$. The semiconductor tracker detectors are silicon strips covering out to $|\eta| < X$ in the barrel region and $|\eta| < 2.5$ in the forward regions. The transition-radiation tracker covers $|\eta| < 2$ with straw tubes in both the barrel and forward regions. The ATLAS calorimeter has large coverage in pseudorapidity ($|\eta| < 4.9$) and longitudinal segmentation in both electromagnetic and hadronic sections. In the barrel region, the electromagnetic calorimeter has three layers and a presampler layer, all using liquid argon technology. The first layer has very high resolution in the η direction, allowing discrimination of photons from neutral hadron decays. The second layer is coarser but deeper, providing the primary energy measurement for electromagnetically interacting particles (photons and electrons), while the third layer is there to catch the tails of the deposited electromagnetic showers. The ATLAS hadronic calorimeter uses steel absorber and measures the hadronic showers by means of scintillating tiles. In the endcap region, beyond $|\eta| = 2$, both hadronic and electromagnetic sections use LAr technology with relativly coarse cell segmentation. The
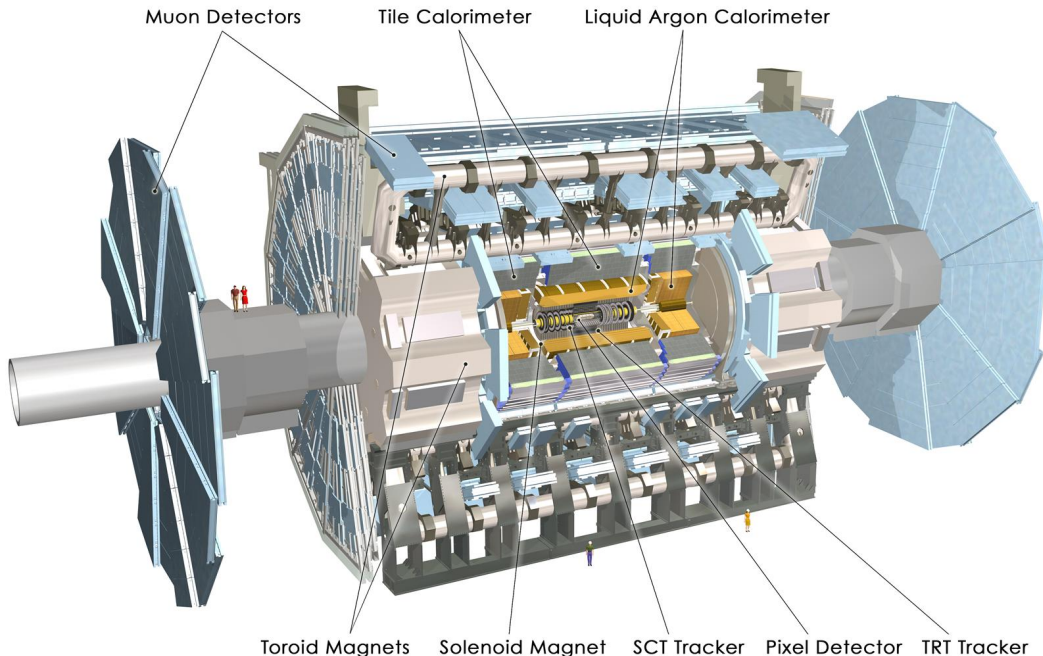
Figure 2: Schematic view of ATLAS detector at the LHC, highlighting the major subsystems.

ATLAS forward calorimeter (FCal) covers $|\eta| = 3.2 - 4.9$, using a matrix of copper and liquid argon in the electromagnetic section, and tungsten and liquid argon for the hadronic section. The ATLAS muon spectrometer covers $|\eta| < 2.7$ with precision drift chambers in the barrel region and cathode strip chambers in the forward region. The bending of muons is provided by three air-core toroids, giving a momentum resolution ranging from approximately 2% up to about 10% at $p_T = 1$ TeV.

ATLAS provides a sophisticated multi-level trigger system for selection of physics objects (jets, taus, photons, electrons, muons, and missing transverse energy). Jet triggering is done both seeding on energy deposited into localized regions of the calorimeter, as well as a full reconstruction of the jets using a similar algorithm as used in the offline analysis. Electron and photon triggering uses smaller regions in the calorimeter than for jets, and also applies selections based on the measured shower shape and leakage in the hadronic sections. Muon triggering is provided by thin-gap chambers and resistive plate chambers, covering about 90% of the solid angle out to $|\eta| = 2.7$. In general, triggering on tau leptons and missing transverse energy (e.g. from W bosons) is not utilized for any heavy ion analysis, as both are highly contaminated by the large fluctuations in the underlying event.

2 Event characterization

The first analyses of LHC heavy-ion data dealt with the charged particle density and the energy density achieved in Pb–Pb interactions at an unprecedent collision energy of $\sqrt{s_{NN}} = 2.76$ TeV per nucleon pair in centre-of-mass system. The estimated values, as well as the results of practically all other measurements, strongly depend on the geometry of the collision (also called centrality), more precisely on the distance b of the centres of colliding nuclei in the plane transverse to the beam axis, called impact parameter of the collision. The impact parameter determines the volume of the interaction region, i.e. how violent the collision was. In this Section we first describe how the centrality of Pb–Pb collisions is determined, and then we turn to the basic measurements which characterize these interactions at the LHC.

2.1 Centrality determination

The lead nuclei are relatively extended objects, their size is about 14 fm across. To classify events according what part of the two nuclei participated in the interaction, the concept of collision centrality is commonly introduced in the field of heavy-ion physics. The centrality of the collision can be expressed in terms of geometrical parameters, such as the impact parameter b, or the number of participating nucleons. These parameters are inferred by comparison of experimental data with simulations of interactions. In this context the geometrical Glauber model is typically used [?], based on a description of pA and A–A scattering, originally proposed by R.J. Glauber [?, ?]. For the event simulation a Monte Carlo implementation of Glauber model is exploited [?, ?], which is realized by the following steps:

- randomly sample the position of each nucleon inside the nucleus according to a Woods–Saxon distribution (two-parameter Fermi distribution), using the parameters extracted from the analysis of low-energy elastic e–A scattering [?];

- randomly sample the collision impact parameter b with probability distribution $P(b) \propto b \, db$ (up to $b_{\mathrm{max}} = 20$ fm, i.e. well above the lead nucleus diameter);

- assuming nucleons are moving along straight lines parallel to the beam direction, a pair of nucleons is considered as colliding if their centres are closer than $\sqrt{\sigma_{\mathrm{NN}}/\pi}$ in the transverse plane, where $\sigma_{\mathrm{NN}} = (64 \pm 5)$ mb is the inelastic nucleon–nucleon cross section, estimated from LHC pp measurements;

and for each event the number of nucleons participating in at least one collision (N_{part}) and the number of these binary collisions (N_{coll}) are counted. Then the total nuclear Pb–Pb cross section (σ_{PbPb}) is calculated as the fraction of πb_{max}^2 given by the ratio of the number of events with $N_{\mathrm{coll}} \geq 1$ to the number of all generated events. The cross section for collisions with impact parameter in the interval $(0, b)$ is obtained the same way, counting the events with $N_{\mathrm{coll}} \geq 1$ having the impact parameter within that interval. The centrality for this impact-parameter selection is its cross section expressed as the percentage of σ_{PbPb}. A centrality class is defined by its lower and upper percentages, corresponding to the events within impact-parameter interval $(b_{\mathrm{l}}, b_{\mathrm{u}})$, where the lower percentage is the part of σ_{PbPb} up to the impact parameter b_{l} and the upper percentage is that part up to b_{u}. Other characterizations of centrality classes, such as the mean number of participants $\langle N_{\mathrm{part}} \rangle$ and the mean number of binary collisions $\langle N_{\mathrm{coll}} \rangle$ (obtained as the average values for events within that class) are also employed. For completeness, the geometrical overlap function (integral of the convolution of the two transverse nuclear densities in the overlapping region) in the Monte Carlo formulation of Glauber model is defined as $T_{\mathrm{AA}} = N_{\mathrm{coll}}/\sigma_{\mathrm{NN}}$.

However, none of the geometrical quantities mentioned above (b, N_{part}, N_{coll}) is directly measurable in an experiment. Therefore, an experimental observable, which strongly correlates with the collision impact parameter, has to be used to classify the events according to their centrality. For example, the charged-particle multiplicity N_{ch} (or the energy deposition in a calorimeter) within a given pseudorapidity region is often used. In what follows the centrality determination as implemented by the ALICE collaboration is described [?], and later the differences for other experiments are mentioned. The centrality selection of events within a certain impact-parameter interval is then replaced by a selection using a N_{ch} interval. In an ideal case, if one were able to measure the event distribution in such new selection variable for all Pb–Pb nuclear collisions, it would be possible to define centrality selection and centrality percentiles without any model, using only this distribution and its integral. However, for very peripheral collisions (large b, low N_{ch}) the experimental event sample is contaminated by electromagnetic interactions, at LHC energies these processes have a huge cross section (more than two orders of magnitude larger than the nuclear cross section) and contribute to low multiplicity events [?, ?]. It is necessary to suppress them, at least partly, already during the data taking (triggering on a minimum multiplicity
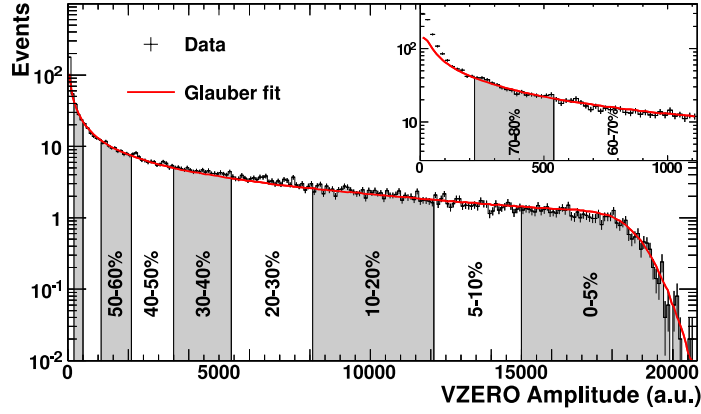
Figure 3: Distribution of the sum of amplitudes from the VZERO scintillators in the ALICE experiment (histogram) fitted to Glauber Monte Carlo coupled to NBD multiplicity production model (line). The inset shows peripheral-collision region enlarged. Reproduced from [?].

value, or requiring some signal in ZDC's, see Sec. 1.3), which inevitably makes the event trigger less efficient for very peripheral collisions. For these reasons, the event distribution in a variable such as N_{ch} is usable for centrality selection only above some value, typically excluding peripheral collisions corresponding to the centrality class 90–100 %, where the contamination and the trigger inefficiency cannot be neglected. In order to determine the value, from which the distribution can be used, and to relate this so-called anchor point to the centrality, two approaches are utilized. The simulation of the Pb–Pb electromagnetic processes together with the experiment's trigger response gives the possibility to correct the event distribution of the selection variable, and to estimate a reasonable position of the anchor point with its centrality. Alternatively, the Glauber Monte Carlo can be supplemented with a model of particle production, describing the experimental selection-variable distribution and finding the point where the two deviate. Such an approach also allows to calculate for a given centrality selection the corresponding $\langle N_{part} \rangle$ and $\langle N_{coll} \rangle$, taking into account the finite resolution of the selection variable N_{ch} with respect to the collision impact parameter b.

A simple model for multiplicity production, exploited together with a Glauber Monte Carlo, consists in the simulation of the multiplicity distribution from one particle source and a prescription for the number of particle sources depending on the collision geometry, called the number of ancestors (N_{anc}). For the multiplicity distribution the Negative Binomial Distribution (NBD) is typically used, it has two parameters (controlling the mean and width), and describes reasonably well the charged-particle multiplicity in different pseudo-rapidity windows for high-energy pp interactions. The number of particle sources is parameterized as a function of N_{part} and N_{coll}, the common choice being $N_{anc} = fN_{part} + (1 - f)N_{coll}$, motivated by a two-component model, where the number of sources is composed of soft (proportional to N_{part}) and hard (proportional to N_{coll}) interactions. Thus, such a model has three parameters, two for the NBD and f for N_{anc}, which are fitted to the experimental distribution of the selection variable between the anchor point and the maximal value (most central collisions).

Figure 3 illustrates the result of such a fit to the event distribution of the sum of amplitudes from the VZERO counters (see Sec. 1.3 for detector description) in the ALICE detector. This variable is proportional to the multiplicity in the pseudo-rapidity region covered by the VZERO detector. The centrality classes and their percentiles are determined by integrating the experimental distribution from its maximal value down to the anchor point. Simulated events are then used to calculate $\langle N_{part} \rangle$ and $\langle N_{coll} \rangle$ for the centrality classes. The ATLAS experiment for the centrality selection is using transverse energy measured in Forward Calorimeters (FCal) and, instead of the model for multiplicity production, the pile-up of calorimeter response from N_{anc} pp collisions is exploited [?]. The CMS experiment bases its Pb–Pb centrality selection on Hadron Forward (HF) calorimeter, and the distribution of the transverse-

energy sum is corrected with the simulation of the trigger response [?]. Another detector commonly used for centrality measurements is the ZDC. Its disadvantage is that, unlike for the multiplicity-type detectors, the ZDC response is not a monotonic function of centrality: it gives small signals both for very central and for very peripheral collisions. ZDC's are therefore normally used in correlation with some other detector, especially for central and very central events.

The centrality determination and its uncertainties affect practically all the results from the analyses of heavy-ion data. A careful systematic study of the centrality selection dependence on different assumptions is always required. This usually includes: variation of the parameters describing the nucleus density; including or not a minimal separation between nucleons inside each nucleus; modifying the definition of colliding nucleons (from a black-disc assumption to a Gaussian profile description, or introducing an intra-nuclear rescattering); and changing the functional dependence of N_{anc}, if used, to a power function of N_{part} or N_{coll}. All these uncertainties must then be properly propagated to the measurements of other quantities.

2.2 Charged-particle density

Traditionally, the very first measurements of heavy-ion collisions at a new energy regime comprise the charged-particle density, and its centrality dependence. These measurements were performed by all three experiments participating in the LHC heavy-ion programme [?, ?, ?, ?], and the first results were published already during the first heavy-ion run [?]. The methods exploited to measure the charged-particle density ($\mathrm{d}N_{\mathrm{ch}}/\mathrm{d}\eta$) in the mid-rapidity region ($|\eta| < 0.5$) were very similar. All experiments used their silicon pixel trackers, detectors closest to the interaction point, to count so called tracklets, pairs of reconstructed hits (pixel clusters) in two layers of the pixel detectors aligned with the primary vertex. Other methods, such as measuring the cluster multiplicity, partial tracking with innermost detectors, and TPC tracking (in the case of ALICE), were also utilized. The collision-energy dependence of $\mathrm{d}N_{\mathrm{ch}}/\mathrm{d}\eta$ for the most central heavy-ion collisions, normalized per participant pair (i.e. $\langle N_{\mathrm{part}}\rangle/2$), is presented in Fig. 4, top part. The results from the three experiments are in excellent agreement, and they show an increase by more than factor of two, compared to the highest value observed at RHIC. The energy dependence of the charged-particle density can be satisfactorily parameterized by a power function: $\propto s_{\mathrm{NN}}^{0.15}$. Note that the energy dependence for heavy ions is significantly steeper than that for pp interactions ($\propto s^{0.11}$), this is also reflected by the more than a factor two higher value of the normalized charged-particle density ($\mathrm{d}N_{\mathrm{ch}}/\mathrm{d}\eta)/(0.5\langle N_{\mathrm{part}}\rangle)$ in heavy-ion collisions compared to pp interactions. It is interesting to note that most of the theoretical and model predictions for the LHC charged-particle density underestimated the experimental observation [?], contrary to a clear tendency for an overestimation when the first results from RHIC experiments were published.

In the bottom part of Fig. 4 the centrality dependence of the same quantity ($\mathrm{d}N_{\mathrm{ch}}/\mathrm{d}\eta)/(0.5\langle N_{\mathrm{part}}\rangle)$, expressed as a function of $\langle N_{\mathrm{part}}\rangle$, is presented. Again, very good agreement among the three LHC experiments is observed. The data from RHIC (average value over the four experiments [?]) are also shown, multiplied by a factor 2.15 to match the points for the most central collisions. The normalized charged-particle density is rising with centrality, which means that the particle multiplicity at mid-rapidity increases faster than the number of participants, presumably due to the contribution of hard processes to the multiplicity production. However, this increase is very similar to that observed at the top RHIC energy. Apart from a simple interpretation of these data in terms of (a mixture of) soft and hard interactions, model calculations implementing a saturation picture, where the number of soft gluons available for the multiplicity production is progressively reduced by parton recombination, attempt to determine the energy and centrality dependence of the saturation scale [?, ?, ?].

The experiments were also looking for the $\mathrm{d}N_{\mathrm{ch}}/\mathrm{d}\eta$ evolution in the longitudinal direction, i.e. as a function of pseudo-rapidity. The ATLAS collaboration published the charged-particle densities for different centrality classes in $|\eta| < 2$ [?], and the CMS detector measured $\mathrm{d}N_{\mathrm{ch}}/\mathrm{d}\eta$ in the interval
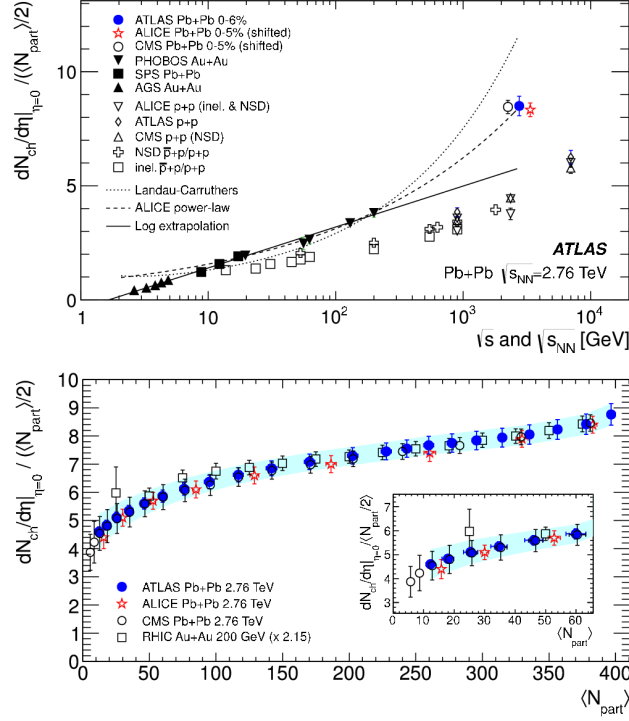
Figure 4: Top: Energy dependence of the charged-particle density at mid-rapidity ($|\eta| < 0.5$) normalized per participant nucleon pair, from various pp (and $\bar{p}p$) measurements, and most central heavy-ion collisions. The curves represent various extrapolations from lower-energy data to LHC, the one describing heavy-ion experimental points (dashed line) is a power function $(\mathrm{d}N_{\mathrm{ch}}/\mathrm{d}\eta)/(0.5\langle N_{\mathrm{part}}\rangle) \propto s_{\mathrm{NN}}^{0.15}$ proposed in [?]. Bottom: $\langle N_{\mathrm{part}}\rangle$ dependence of the charged-particle density normalized per participant nucleon pair from the three LHC experiments, compared to average value from RHIC experiments, multiplied by a factor 2.15. The inset shows in detail the peripheral-collision region with $\langle N_{\mathrm{part}}\rangle < 60$. Reproduced from [?].
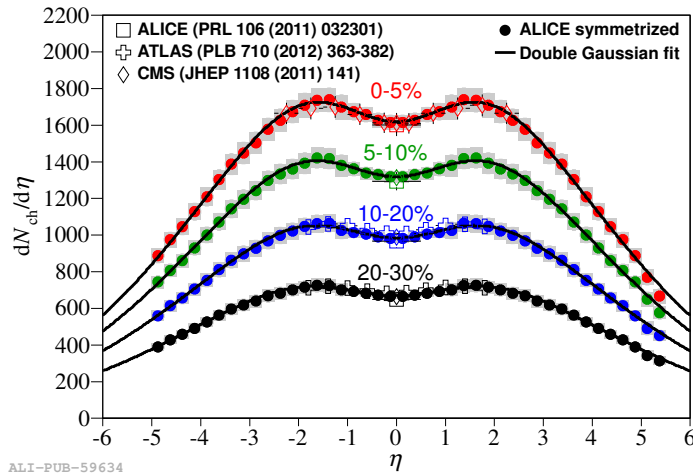
Figure 5: Charged-particle pseudo-rapidity density distribution for various centrality classes, comparison among the LHC experiments. Reproduced from [?].

$|\eta| < 2.5$ [?]. The ALICE experiment extended the pseudo-rapidity coverage of such measurement to $-5 < \eta < 5.5$ [?], exploiting the FMD (see Sec. 1.3) and so called satellite bunches. The latter are created in the accelerator RF cavities, when a small fraction of particles slips from the main bunch into another wave period, 75 cm apart (corresponding to RF frequency 400 MHz). This way, very low-intensity satellite collisions, distanced by every 37.5 cm from the main bunch crossing, are produced, shifting the pseudo-rapidity acceptance. Figure 5 shows the results of the ALICE pseudo-rapidity distribution measurement, compared to the data previously obtained by CMS and ATLAS. The wide-rapidity data are used together with the RHIC results (from the BRAHMS [?] and PHOBOS [?] experiments) to confirm limiting fragmentation — the shape of the distributions are in the fragmentation region independent of the collision energy. By extrapolation, the total charged-particle multiplicity in Pb–Pb collisions at $\sqrt{s_{NN}} = 2.76$ TeV for different centralities can be estimated, for example, in 5 % of the most central events $(17.2 \pm 0.8) \times 10^3$ charged particles are created.

2.3 Energy density

In order to estimate the energy density achieved in Pb–Pb collisions at the LHC, the measurements of the transverse energy pseudo-rapidity density, $dE_T/d\eta$ were performed. The CMS experiment measured directly the energy flow in calorimeters for different pseudo-rapidities and centralities [?]. The collision energy dependence of $dE_T/d\eta$ at mid-rapidity for the most central heavy-ion collisions, normalized to the the number of participant pairs, is shown in Fig. 6. An increase by more than a factor three is observed from the top RHIC energy to the LHC. This collision-energy dependence can be satisfactorily described by a power function $\propto s_{NN}^{0.2}$, which means that the transverse-energy density rises with collision energy faster than the particle density, indicating a significant increase of the average transverse momentum of particles produced in the LHC heavy-ion interactions. The ALICE experiment confirmed the CMS results estimating $dE_T/d\eta$ from $dN_{ch}/d\eta$ and the measured transverse-momentum spectra for different hadron species.

Even in forward region, up to $|\eta| = 5$, the transverse-energy density observed at the LHC is larger than that at mid-rapidity at the top RHIC energy. The energy density achieved in heavy-ion interactions (ϵ) is commonly related to the transverse-energy density by the Bjorken formula [?], based on geometrical considerations. It can be expressed as $\epsilon \tau_0 = (dE_T/dy)/S$, where τ_0 denotes the time when the initial thermalization was established (supposed to be $\tau_0 \leq 1$ fm), and S is the transverse overlap area, approximated for central Pb–Pb collisions with $\pi(7\,\mathrm{fm})^2$. For the top 5 % centrality CMS obtained
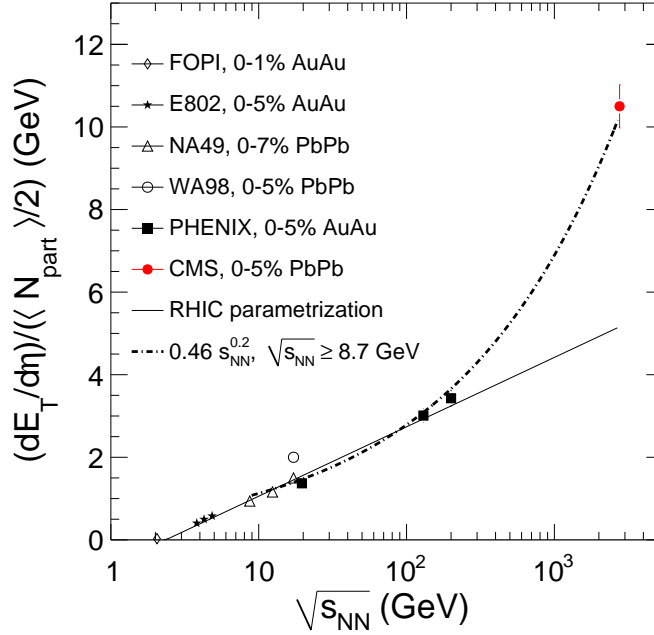
Figure 6: Collision energy dependence of the transverse-energy pseudo-rapidity density at mid-rapidity, normalized to the number of participant pairs, for central heavy-ion collisions. The curves represent various extrapolations from lower-energy data to LHC, the one describing the LHC measurement (dashed–dotted line) is a power function $(\mathrm{d}E_\mathrm{T}/\mathrm{d}\eta)/(0.5\langle N_\mathrm{part}\rangle) \propto s_\mathrm{NN}^{0.2}$ proposed in [?], from where this figure is reproduced.

$\epsilon\tau_0 = 14$ GeV/fm^2 (using a model estimation for Jacobian $\mathrm{d}\eta/\mathrm{d}y \approx 1.1$). This represents a factor 2.6 increase with respect to the highest RHIC collision energy, and an even larger increase for the energy density ϵ, since the time τ_0 is expected to be shorter at the LHC.

3   Particle spectra and yields

3.1   Charged-particle transverse momentum spectra

Transverse momentum spectra of charged particles were measured by all three experiments exploiting the first collected data sample. They are presented as the dependence of the (inclusive) invariant cross section on the transverse momentum (p_T), and finally in the form normalized to pp measurement at the same nucleon–nucleon energy. For the latter representation, the nuclear modification factor is defined as

$$R_\mathrm{AA}(p_\mathrm{T}) = \frac{\mathrm{d}N_\mathrm{ch}^\mathrm{AA}(p_\mathrm{T})/\mathrm{d}p_\mathrm{T}}{\langle N_\mathrm{coll}\rangle\, \mathrm{d}N_\mathrm{ch}^\mathrm{pp}(p_\mathrm{T})/\mathrm{d}p_\mathrm{T}}, \tag{1}$$

where on the right hand side the superscripts AA and pp refer to the values obtained in heavy-ion and pp measurements, respectively. If a collision of two nuclei behaved as a simple superposition of N_coll nucleon–nucleon collisions, the nuclear modification factor would be $R_\mathrm{AA} = 1$. Such a scaling with the number of binary collision N_coll is a natural expectation for hard processes, in case that nucleons act independently and their interactions are not influenced by the rest of the nuclei. A deviation of R_AA from unity for hard processes signals a nuclear effect. However, for soft processes, such as particle production at p_T below a few GeV, the scaling from pp to AA is governed by N_part rather than by N_coll leading to a higher R_AA in that p_T region, especially for central events.
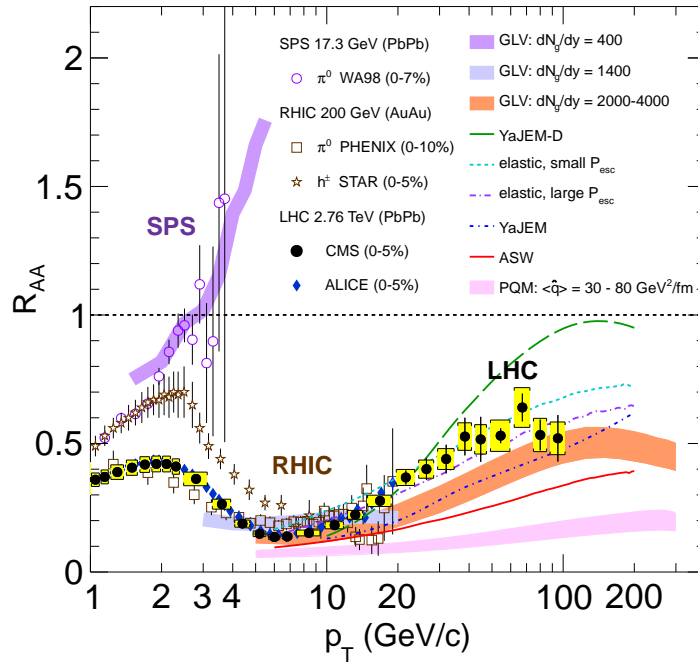
Figure 7: Transverse momentum dependence of nuclear modification factor R_{AA} for charged particles produced in central heavy-ion collisions at LHC and lower energies. The curves and bands represent different model calculations. Reproduced from [].

The p_T spectrum for charged particles in LHC heavy-ion collisions was expected to be suppressed at high p_T with respect to pp interactions. The fact that R_{AA} is significantly below unity at p_T above a few GeV was well established for central collisions at RHIC, and attributed to the jet quenching — an energy loss of hard partons in their interactions with the surrounding high-density nuclear matter. As the high p_T particles are supposed to be produced in the fragmentation of such hard partons, their quenching lowers the particle production, reflecting the amount of energy loss, and thus the density of nuclear matter created in the collision. However, the value of R_{AA} is also dependent on the steepness of the parton p_T spectrum (a harder parton spectrum at the LHC should result in less particle suppression), and on the nuclear modification of the structure functions (distribution of partons inside a nucleon). Therefore, for theoretical predictions and interpretations of the R_{AA} behaviour, model calculations taking into account the interplay of many effects are necessary.

The first LHC measurement of charged-particle R_{AA}, was published by ALICE, presenting the p_T spectrum up to 20 GeV, for the 5 % most central Pb–Pb events. It showed a slightly stronger suppression compared to RHIC: the largest suppression — in the p_T range 6–7 GeV — was a factor about 7 at the LHC, while at RHIC a factor of 5 was observed. A new observation was that with increasing p_T the suppression gets smaller, i.e. R_{AA} increases. This was soon confirmed by the CMS measurement [], extending the p_T reach up to 100 GeV (see Fig. 7). The nuclear modification factor R_{AA} exhibits a clear increase up to p_T about 40 GeV, and and then seems to saturate with the R_{AA} value about 0.5–0.6 for the most central collisions. Figure 7 also shows the p_T dependence of R_{AA} at lower energies, and a variety of model calculations. Different models can be tuned to fairly reproduce the R_{AA} data, however, it remains to demonstrate that they describe with the same parameters the ensemble of other observables, especially the azimuthal anisotropy (Sec. 5).

The ALICE and CMS experiments also measured the R_{AA} p_T dependence for different collision centralities. The charged-particle production is, as expected, less and less suppressed as one moves from central to peripheral Pb–Pb collisons. The ATLAS collaboration reported similar results, presented as R_{CP} as a function of p_T, where R_{CP} stands for a quantity analogue to that defined in Eq. 1 using the
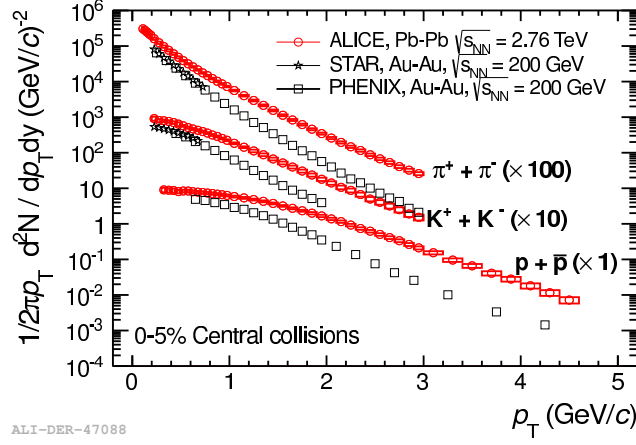
Figure 8: Transverse momentum spectra for pions, kaons, and protons (sum of particles and antiparticles) produced in 5 % of most central Pb–Pb collisions at LHC, compared to the RHIC measurements. Reproduced from [].

normalized ratio of heavy-ion results at different centralities (the subscript CP indicates the central-to-peripheral ratio), commonly using the most peripheral class available for normalization.

3.2 Identified-hadron spectra

Study of the particle composition as a function of p_T reveals a mass hierarchy, interpreted as resulting from a common radial-velocity field created during the expansion of the dense-matter fireball. Such a collective flow arises in strongly interacting matter in the presence of a pressure gradient. Having the same velocity, heavier particles (e.g. protons) will acquire a larger momentum than lighter mesons. This effect is clearly visible in Fig. 8, where the p_T spectra for pions, kaons, and protons measured by the ALICE experiment [] exploiting various particle-identification techniques, are presented for the top 5 % central events. From the simultaneous blast-wave fit to these spectra (excluding pions with $p_T < 0.5$ GeV and kaons with $p_T < 0.35$ GeV where resonance decays largely contribute), the kinetic freeze-out temperature (T_{kin}, temperature when the hadrons cease to interact) and an average radial velocity ($\langle \beta \rangle$) is estimated. The two parameters were extracted for different centralities, and they were found to be strongly correlated, since they both determine the slope of the p_T spectra. Both T_{kin} and $\langle \beta \rangle$ are higher compared to RHIC, and they depend on centrality: T_{kin} being lower for more central collisions, while $\langle \beta \rangle$ increases. The values reached for 5 % of most central collisions are $T_{kin} \approx 95$ MeV and $\langle \beta \rangle \approx 0.65$, the latter being more than 10 % above the RHIC value. These spectra were compared further to various hydrodynamical-model calculations [], and a fair description for the bulk production, up to transverse momenta 2–3 GeV, i.e. where such models are applicable, is observed for central collisions. In some cases [] the agreement is improved by supplementing the hydrodynamical calculations with a hadronic rescattering code (UrQMD [], in this occasion). But going to more peripheral collisions the hydrodynamical description becomes worse.

The p_T spectra of identified charged hadrons are determined up to $p_T = 20$ GeV, exploiting the measurement of ionization energy losses in the ALICE TPC in the relativistic rise region. Figure ?? presents these results normalized to the pp baseline, as R_{AA} for pions, kaons, and protons, compared to the (averaged) charged-particle data. It is clearly seen that for p_T above 7–8 GeV the behaviour for all particle species coincides. For lower p_T a mass hierarchy appears: the heavier the particle, the lower its suppression. These observations suggest the presence of three regions in transverse momentum:

- bulk region, low p_T up to 2–3 GeV, where the production comes from the hadronization of high-

density strongly-interacting matter created in a heavy-ion collision, reflecting collective radial flow, fairly described (at least for central collisions) by hydrodynamical models;

- intermediate region, in p_T up to 7–8 GeV, where still a mass splitting among various particle species persists that can be attributed a reminiscence of radial flow (the difference has to disappear for p_T values significantly larger than particle masses), however, additional ideas were put forward to push further in p_T this mass distinction, such as constituent-quark recombination which would favour baryons to acquire larger p_T than mesons;

- fragmentation region, above 7–8 GeV in p_T, where the different hadron species exhibit a common suppression pattern, and consequently their relative abundances are the same as in pp collisions, naturally explained as being fragmentation products of a high-p_T parton coming from a hard scattering at early stage (which itself is quenched by the surrounding high-density matter).

To look in detail into the intermediate region, it is instructive to plot the proton-to-pion ratio as a function of p_T, fig. **??**. The striking effect is that for central collisions at p_T around 2.5–3 GeV this ratio is more than a factor three higher than the value for pp collisions. This so-called baryon anomaly was observed already at RHIC, and certainly the low-p_T rise is explained by the hydrodynamical radial flow. In the intermediate region, where the hydrodynamics ceases to work, the behaviour is qualitatively described by models involving constituent-quark recombination or baryon string-junction transfer along the axis of a fragmenting jet. These models, however, tend to predict an anomalous baryon-to-meson ratio even for significantly higher p_T than actually observed. On the other hand, a smooth connection between the hydro-described bulk region and the normal-ratio fragmentation region, using a realistic radial-flow profile, will probably move the border between the intermediate and fragmentation regions to lower than observed values. Therefore, a comprehensive description of the particle production in the intermediate region is still an open, and experiment driven issue.

3.3 Strange-particle production

Historically, the enhancement of strangeness production was among the first signatures proposed to signal a qualitatively different state of matter, expected to be created in ultra-relativistic heavy-ion collisions []. The strangeness increase in high-temperature QCD matter is motivated by two reasons: the relevant quark masses drop from their constituent to their bare values, and then the strange-quark mass becomes comparable to the temperature, consequently the production rates for different light quarks tend to equalize. Strangeness enhancement was already observed at lower energies, at the SPS [], as well as at RHIC []. The systematic study of strangeness production at the LHC is under way in ALICE. In addition to charged kaons, the measurements include topologically identified particles (K_s^0, Λ, Ξ^-, and Ω^-), and resonances containing strangeness.

The enhancement of strangeness production is confirmed at the LHC, see Fig. **??**, albeit the enhancement factor, expressed as the ratio of the yield per participant in A–A collisions to that in pp (or pA) collisions, decreases slowly with the collision energy. This reflects the fact that the production of strange particles per pion in heavy-ion collisions practically saturates as $\sqrt{s_\mathrm{NN}}$ reaches few tens of GeV, while in pp it still increases from RHIC to the LHC, and only at the highest energy ($\sqrt{s} = 7$ TeV) seems to cease its growth.

The strange-particle R_AA is also influenced by strangeness enhancement, especially in the bulk and intermediate p_T regions. As already mentioned, kaons, including K_s^0, are above the pion curve. The strange baryons have larger R_AA than protons, and R_AA increases with the strangeness content, exceeding unity for Ω^-. With increasing p_T, the strangeness R_AA goes progressively closer to the common fragmentation behaviour for all other particle species, still being for Ω^- at $p_\mathrm{T} \approx 7$ GeV above the others. These measurements are at this point limited by the available statistics.

Baryon-to-meson ratio in the strangeness sector is very similar to that of proton-to-pion. The Λ-to-K_s^0 ratio as a function of p_T is shown in Fig. **??** together with hydrodynamical- and recombination-model calculations. The EPOS model [], which includes the hydrodynamical expansion and, at higher p_T, the (mini-)jet fragmentation with an interaction between jets, describes the experimental measurement fairly well.

3.4 Resonance and light-nuclei production

The resonances are interesting to study in heavy-ion collisions, because of their short lifetime they may decay inside the medium, before the kinetic freeze-out. If a decay product scatter changing its momentum, the parent resonance cannot be observed by invariant-mass reconstruction, and that leads to an apparent depletion of the resonance yield, which is dependent on the resonance lifetime. On the other hand, resonances can be also recreated during the elastic scattering phase having a large cross-section for s-channel production at very low energies. Therefore, the comparison of the different-lifetime-resonance yields with hadronic-transport models gives valuable information about the time evolution during the late stage of heavy-ion collisions.

At the LHC, the ALICE collaboration reported the measurements of $K^*(892)^0$ and ϕ mesons. The yield of K^{*0} relative to other particles (e.g. K^-) decreases significantly for more central collisions, while the ϕ yield normalized in the same way is compatible with being independent of centrality. This is qualitatively understood by an order of magnitude different lifetimes for the two resonances (4.2 fm and 46 fm for K^{*0} and ϕ, respectively). A substantially lower production of K^{*0} in central collisions also means that the regeneration is not effective enough to compensate the decay rate. Similar observations were made at RHIC []. The ϕ meson, being relatively long-lived to be treated as stable on the time scale of the heavy-ion collision, is of special interest. Its mass is close to that of the lightest baryons, therefore, the ϕ p_T spectrum can differentiate mass-dependent effects and constituent-quark-number effects. Preliminary data indicates compatibility between proton and ϕ p_T spectra up to 5 GeV, favouring thus the radial-flow explanation of the baryon anomaly to the constituent-quark-recombination one.

The high density of particles produced in heavy-ion collisions implies substantial rates for light-nucleus and hypernucleus production. The interest of such measurement is to study the production mechanism of such state, their coalescence coefficients, and their thermodynamical equilibrium with other particles. The light nuclei, such as d, t, ^{3}He, and ^{4}He, and corresponding antinuclei, were observed in heavy-ion collisions at RHIC and the LHC, and quantitative results for d and ^{3}He were reported by ALICE. These measurements use the particle identification based on the specific ionization losses in TPC and the TOF measurement. The production of hypernuclei (nuclei containing one ore more strange baryons) is of additional interests since the (unknown) properties of hypernuclei, their masses and decays, can be measured. The ALICE collaboration reconstructed the $^3_\Lambda$H $\rightarrow ^3$He $+ \pi^-$ decays, as well as the charge-conjugated ones, opening the study in this field at the LHC, following the first antihypertriton measurement at RHIC []. Searches for more exotic states, such as the H-dibaryon ($\Lambda\overline{\Lambda}$ bound state or six-quark state), the $\overline{\Lambda\mathrm{n}}$ bound state, and the $\Phi(1860)$ pentaquark have not given any positive signal.

3.5 Particle yields

The particle yields at mid-rapidity are obtained by integration of the transverse-momentum spectra fitted to the blast-wave functional dependence (or other suitable function), in order to extrapolate below the lowest measured p_T. Traditionally, the particle yields in heavy-ion collisions are studied within statistical hadronization models. These models are based on the grand-canonical ensemble, describing the system with the temperature (T_{ch}), the baryon chemical potential (μ_b), and the volume

in thermal and chemical equilibrium with the rest. Knowing these parameters it is straightforward to calculate the average number of various particles in the system. All the resonance and other unstable states, summed-up in the grand potential (usually with an upper mass cut-off about 2 GeV, as above the resonance spectrum is not well known), are decayed into observed particles and compared to the measurements. The temperature T_{ch} is interpreted as the chemical freeze-out temperature, below which the energy of hadronic re-scattering is lower than the threshold for inelastic interactions, and thus the particle composition remains unchanged.

The statistical models were used to describe the heavy-ion collision data from very low energies up to RHIC with a good agreement for most of the particle species. The temperature T_{ch} practically does not change with the collision energy, therefore, a reasonable estimate for LHC is the value observed at RHIC, $T_{ch} = 164$ MeV; the chemical potential has to be very low as the ratio particles to antiparticles is for all species compatible with unity; $\mu_b = 1$ MeV is usually assumed. The predictions using these parameter values are compared in Fig. **??** with the measurements of yield ratios: p/π and K/π, for different centralities (expressed by particle density). The conclusion is that the measured proton yield for central Pb–Pb collisions at the LHC is by a factor of about 1.5 lower than predicted. In order to describe the proton measurement, significantly lower T_{ch} is needed (about 152 MeV), but then the yields of multi-strange baryons are underestimated. Trying to fit the temperature to the available data gives an estimate of $T_{ch} \approx 156$ MeV, however, the fit description is not as good as it was at lower energies. Moreover, it is hard to expect that the chemical freeze-out temperature would decrease at higher energy.

It Seems that such problems were there partly already at RHIC. The discrepancy being smaller, and uncertainties in proton-yield corrections, lead to the fact that it was considered not significant. There are few attempts to explain the lower proton yield at the LHC:

- The baryons can annihilate in re-scattering with antibaryons, even after chemical freeze-out. This will affect protons more then strange baryons, because protons have larger density, and the annihilations with a strange partner are penalized due to presence of kaon(s) in final state, which shrink the phase space and thus lower the cross section of such cross-flavour annihilation. The effect was confirmed with UrQMD calculations [], and the particle density makes it larger at the LHC than at RHIC. It was also shown that multi-meson interactions, recreating the baryon–antibaryon pairs, are not, at decreasing temperature, effective enough to compensate the loss [].

- The statistical hadronization model assumes strictly the same T_{ch} for all particles, which may not necessarily be true. Motivated by recent lattice QCD calculations, flavour- and mass-dependent prehadronic states in QGP may alter the effective phase-transition temperature resulting in an non-uniform freeze out. This will consequently modify the yields predicted by the model.

- The high-mass resonances, not accounted for in the model, would presumably increase mostly the pion yield. Because of the number of these resonances can raise exponentially with the mass [**?**], even their production being exponentially dumped, the effect may be non-negligible. This would lower the p/π model prediction [**?**].

- The statistical hadronization model can be modified, incorporating non-equilibrium effects. In fact the model was used also to describe particle yields in pp, and even in e^+e^-, interactions, however, an additional parameter suppressing strangeness production had to be used. Introducing two parameters regulating the population of phase space, separately for light-quarks and strange quark, allows for good description of the experimental measurements.

The lower-than-expected proton yield observed at the LHC was one of the first surprises from the heavy-ion programme, and its origin has yet to be established.

4 Non-flow correlations

In this Sec. various types of particle correlations, which are not caused by a collective behaviour developed in strongly interacting matter, are discussed. These are typically two-, or a few-, particle correlations arising due to a quantum interference, an interaction between the particles, a common source of production, such as a resonance decay, and a string or (mini-)jet fragmentation. The study of this type of correlations gives information about the space–time evolution of the system, and may shed light on particular production mechanisms.

4.1 Femtoscopic correlations

The term femtoscopy is often employed to indicate methods to measure spatial and time scales at a $\mathcal{O}(1)$ fm level. Basically, two effects are exploited: interference between identical particles and final state particle interactions. The identical particle interference is consequence of the symmetrization of the wave function. It is connected to the Hanbury-Brown and Twiss (HBT) method proposed to measure stellar sizes [], therefore it is sometimes called also in the heavy-ion field HBT method. The production of identical bosons (e.g. pions) with close momenta will be enhanced by such an effect, and that of identical fermions (e.g. protons) will be suppressed. The correlation length in the momentum space is inversely proportional to the spatial size of the source region, assuming that the particles are emitted incoherently. However, the measured correlation is affected by other effects, such as Coulomb interactions, resonance decays, and final state particle interactions, which have to be duly taken into account in the analyses. The latter effect, being often of a short-range nature and present also for non-identical particles, can itself be exploited for femtoscopic studies.

The first results were obtained for like-sign pion–pion correlations with early Pb–Pb data at the LHC []. The analysis was performed in three dimensions, decomposing the relative momentum between the two pions in the longitudinally co-moving system (centre-of-mass system boosted along the beam direction such that the two-pion longitudinal momentum is zero) into its 'out' (direction of the momentum of the pion pair), 'side' (direction perpendicular to the pair momentum and the beam axis), and 'long' (along the beam axis) components. The like-sign two-particle distribution in the three-dimensional relative momentum is normalized to that obtained for pairs of particles from different events (event mixing). At small relative momentum the correlation function exhibits the Bose–Einstein enhancement peak, which is fitted with an expression accounting for the incoherent pion emission from a three-dimensional Gaussian-density source and Coulomb repulsion between particles. As a result the Gaussian HBT radii R_{out}, R_{side}, and R_{long} are extracted. The analysis is performed as a function of k_{T} (one-half of the total pair transverse momentum). The HBT radii are found to be significantly larger (by 10–35 %) than those measured at RHIC, and show a decreasing trend with increasing k_{T}, as also observed in heavy-ion collision experiments at lower energies. This is a characteristic feature of expanding particle sources since the HBT radii describe the homogeneity length rather than the overall size of the particle emitting system. The homogeneity length is defined as the size of the region that contributes to the pion spectrum at a particular momentum.

The energy dependence of the HBT radii is usually expressed as a function of the cubic root of the charged-particle pseudo-rapidity density, i.e. as $(\mathrm{d}N_{\mathrm{ch}}/\mathrm{d}\eta)^{1/3}$. The approximately linear increase (at a given k_{T}) is well-described by hydrodynamical calculations. The product of the three radii, measured at different energies at $k_{\mathrm{T}} = 0.3$ GeV, is shown in Fig. 9 as a function of the charged-particle pseudo-rapidity density $\mathrm{d}N_{\mathrm{ch}}/\mathrm{d}\eta$. This product, multiplied by a factor $(2\pi)^{3/2}$ due to Gaussian distribution normalization, representing then the homogeneity volume, increases linearly with the particle density. At the LHC the homogeneity volume for pion emission for the 5 % most central Pb–Pb collisions doubles compared to that at the top RHIC energy. Within a hydrodynamic scenario the decoupling time for hadrons (τ_{f}, corresponding to kinetic freeze-out) can be extracted from the k_{T} dependence of R_{long}
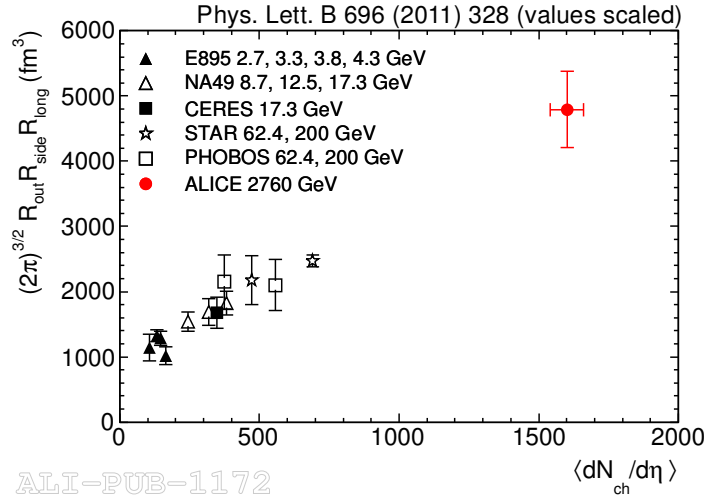
Figure 9: Homogeneity volume for $k_T = 0.3$ GeV as a function of the charged-particle density, measured in heavy-ion collisions at different energies. Adapted from [].
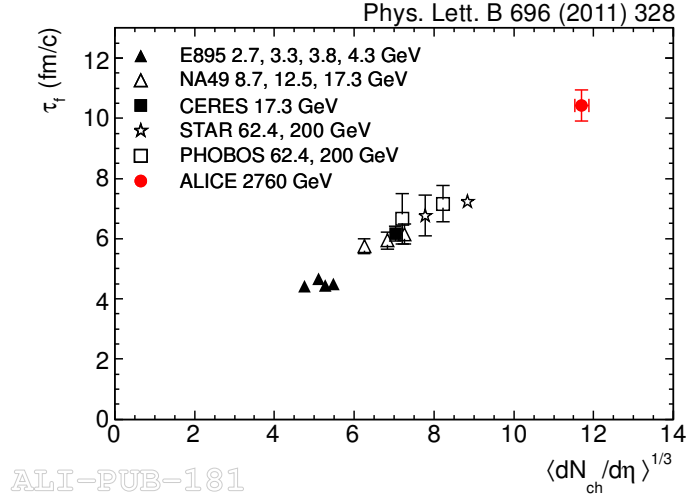
Figure 10: Decoupling time as a function of the cube root of charged-particle pseudo-rapidity density, measured in heavy-ion collisions at different energies. Reproduced from [].

($\tau_f \propto R_{\rm long}$). The decoupling time, estimated this way for different collision energies, is presented in Fig. 10. It increases linearly with $(\mathrm{d}N_{\rm ch}/\mathrm{d}\eta)^{1/3}$, and reaches for most central LHC collisions a value by a factor 1.4 larger than was observed at RHIC. Note that the estimate for τ_f was done for an assumed kinetic freeze-out temperature $T_{\rm kin} \approx 120$ MeV, if one were to use the latest measured value (Sec. 3.2), the decoupling time would increase to 13–14 fm.

In the study of two-pion correlations, the assumption was that the pion emission is incoherent, i.e. the source is fully chaotic. In such conditions the strength of the Bose–Einstein correlations is maximal, and would decrease for a source with a lower degree of chaoticity. Such a situation may be created in heavy-ion collisions, if some kind of condensate would be present or formed (e.g. colour-glass condensate, disoriented chiral condensate). The degree of chaoticity can be assessed comparing two- and three-pion correlations. A recent analysis [] found that the genuine three-pion correlation is suppressed relative to the two-pion correlation, assuming fully chaotic pion emission. This suppression decreases with pion-triplet momentum, and at low momentum (pion $p_T \sim 0.3$ GeV) may correspond to a coherent fraction in charged pion emission of $(22 \pm 12)\,\%$.
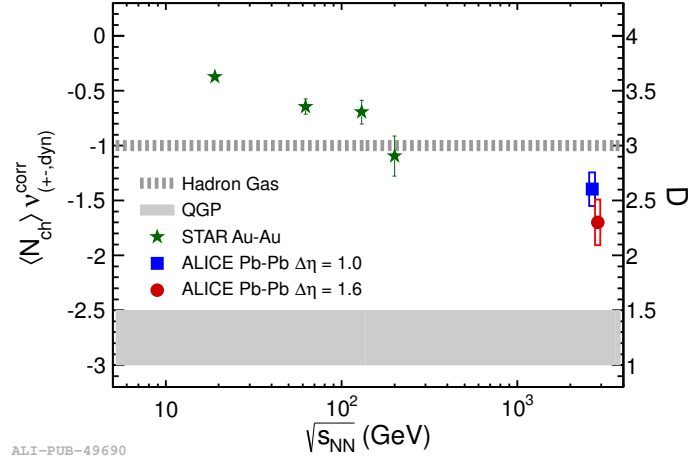
16

Figure 11: Energy dependence of net-charge fluctuations represented as D-measure (defined in the text) in the most central collisions. The two ALICE measurements are for two different pseudo-rapidity intervals $\Delta\eta$ centred around mid-rapidity, and the STAR results are for $\Delta\eta = 1$. The D values are shown on the right-hand ordinate and the shaded areas correspond to the two predictions according the legend. The quantity of the left-hand side ordinate represents the way how the D values are measured, and it is not discussed here. Reproduced from [].

4.2 Fluctuations

Study of event-by-event fluctuations provides a tool to characterize the thermodynamic properties of the system. Such fluctuations are also affected by the system evolution. The fluctuations of conserved quantities in a finite phase space window, such as the net charge of the system, are predicted to be sensitive signals of QGP formation and of the phase transition and may provide an important insight on the properties of strong interactions. In the QGP phase, the charge carriers are quarks with their fractional charges, whereas particles in the hadron phase carry unit charge. The fluctuations in the net charge depend on the squares of the charge states present in the system. Consequently, the net-charge fluctuations in the QGP phase are expected to be significantly smaller compared to those in the hadron phase. The event-by event fluctuations of the net charge in a specific phase-space window (for example a given pseudo-rapidity interval around mid-rapidity) are usually quantified by the D variable, defined as:

$$D = \langle N_+ + N_- \rangle \langle \delta(N_+/N_-)^2 \rangle \approx 4\langle \delta(N_+ - N_-)^2 \rangle / \langle N_+ + N_- \rangle. \tag{2}$$

Here $N_{+,-}$ are the numbers of particles of the two charges in that window, angle brackets denote the average value over the ensemble of events, and δ indicates the variance of the quantity under the square sign. The value of D measures the fluctuation of the net charge $(N_+ + N_-)$ per entropy unit, and is predicted to be around 3 for hadron gas and significantly lower, 1–1.5, for the QGP phase. Figure 11 presents the energy dependence of the D measure obtained by the STAR experiment at RHIC and by ALICE at the LHC in the most central collisions. The fluctuations are expected to be diluted during the medium evolution and thus the D measure may not reach the value predicted for the QGP phase, however, a clear tendency going closer to that prediction with increasing energy is observed.

Event-by-event fluctuations of the mean transverse momentum of charged particles are studied as a function of the charged-particle multiplicity in Pb–Pb collisions with the ALICE experiment, and significant non-statistical fluctuations are observed. The dynamical mean p_T fluctuations arise from correlations among the p_T of the final-state particles, e.g. due to resonance decays, jets, or quantum correlations. To account for such conventional contributions, similar studies are performed in pp, where these correlations are also present. These fluctuations are expected to decrease with increasing

particle density (collision centrality), as $(\mathrm{d}N_{\mathrm{ch}}/\mathrm{d}\eta)^{-1/2}$ under the assumption of independent sources. The measured dependence for peripheral collisions (corresponding to centrality percentiles in the range 60–90 %) follows the pp extrapolation, however, already there the particle-density dependence has a power close to -0.4 instead of $-1/2$. This is interesting, because significant differences in the mean p_{T} are observed between pp and Pb–Pb in that multiplicity range []. At larger particle densities the Pb–Pb fluctuation results deviate from the pp extrapolation: an enhancement in the 40–60 % centrality range is followed by a pronounced decrease for more central events, which indicates a strong reduction of fluctuations towards central collisions. This centrality dependence is compatible with that observed at RHIC. The Pb–Pb data can not be described by models based on independent nucleon–nucleon collisions such as HIJING. Models which include initial state density fluctuations and their effect on the development of collectivity in the final state such as AMPT are in reasonable qualitative agreement with the data. This suggests a connection between the observed transverse momentum fluctuations and azimuthal correlations, and their relation to fluctuations in the initial state of the collision.

4.3 Angular correlations

The angular correlations between two particles are widely used to study various phenomena of both non-flow and collective-flow origin. Here, the method and some applications to non-flow studies is described. The exploitation of the angular correlations for investigation of the azimuthally-dependent flow is explained in Sec. 5. The two-particle correlation between pairs of particles is measured as a function of the azimuthal difference $\Delta\varphi$ (defined usually within $\pi/2$ and $3\pi/2$) and pseudo-rapidity difference $\Delta\eta$. Various kinds of particle pairs are used: they can be all charged particles, pairs selected by charge (like sign, unlike sign), pairs when one particle (trigger) has given p_{T} or type while the second particle (associated) may have some other characteristics, etc. The two-dimensional distribution is constructed for pairs of particles from the same event, and basically two types of the normalization are used: each event is normalized (per number of pairs, or number of triggers) and then the events are summed up, or the events are first summed up and then normalized to the total number (of pairs or triggers). Therefore, one has to be careful, when comparing the results from different experiments, which may have employed different normalization. Then a second two-dimensional distribution is constructed for pairs of particles from the different events (or a trigger particle form one event and all associated from another one). This mixed-event distribution is usually uniform in the $\Delta\varphi$ direction and has a triangular shape in the $\Delta\eta$ direction, reflecting the geometrical acceptance: maximum at $\Delta\eta = 0$, dropping to zero at $\Delta\eta = \pm$ the detector size in pseudo-rapidity. The second distribution is normalized to unity at its maximum (i.e. at $\Delta\eta = 0$), and then used to divide the normalized distribution obtained for particle pairs from the same event. In this way, the acceptance and detection efficiency are taken into account.

An example of such two-dimensional two-particle particle correlation is illustrated in Fig. 12. This is obtained for trigger–associated particle pairs selected according their p_{T} as indicated in the figure. Some typical structures are apparent:

- the peak around $(\Delta\varphi, \Delta\eta) = (0, 0)$ is due to (mini-)jets, sometimes a much narrower peak is also visible on top of that, caused by HBT correlations (for like-sign pairs), or by gamma conversions (for unlike-sign pairs);

- the near-side ridge at $\Delta\varphi = 0$ continuing from the jet peak along the $\Delta\eta$ direction to larger $\Delta\eta$ values, this is presumably caused by the elliptic and higher-harmonic flow (see Sec. 5;

- the away-side ridge at $\Delta\varphi = \pi$ along the $\Delta\eta$ direction, where the second jet may appear (often quenched), now spread along $\Delta\eta$ because the parton–parton system at the origin of the two jets
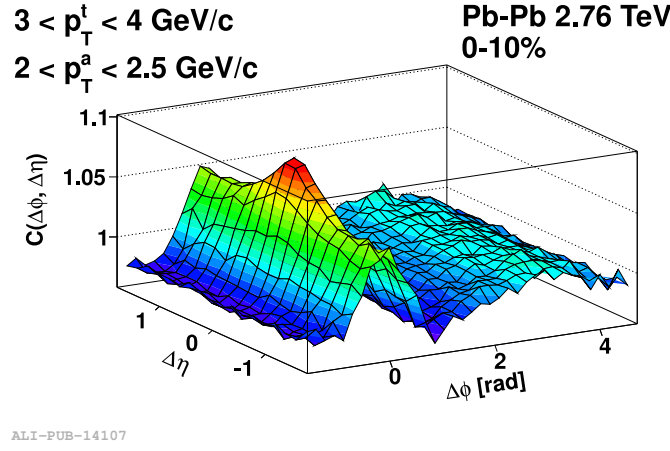
Figure 12: Example of the two-particle correlation function in $\Delta\varphi$ and $\Delta\eta$ for trigger and associated particle selected in p_T intervals displayed in the upper-left corner. The top 10 % of most central Pb–Pb collisions are used. Reproduced from [].

> moves longitudinally with respect to the collision centre-of-mass system, in addition the flow azimuthal modulation also contributes here.

The angular two-particle correlations are analyzed by studying their centrality development, and often by projecting them on one of the axes, excluding or not some structures discussed above.

The two-particle correlations are used to study parton quenching at p_T below $\mathcal{O}(10)$ GeV, where the full jet reconstruction is difficult. In the example shown here the selection requires: a trigger within $8 < p_T^t < 15$ GeV while the associated p_T^a is a variable parameter, respecting $p_T^a < p_T^t$. The two-dimensional correlation is projected on the $\Delta\varphi$ axis in order to measure the number of associated particles correlated to the trigger particle in the near-side and the away-side jet structures. The background from the underlying event, possibly modulated by elliptic flow, has to be subtracted. This is done using three methods: a flat background obtained by the ZYAM (Zero Yield At Minimum) method (the minimum between the near- and the away-side peaks is used to evaluate the background level), a background modulated according the available elliptic-flow v_2 measurements, and a flat background estimated according to the value in the region $|\Delta\varphi| < \pi/2$ and $|\Delta\eta| > 1$ ($\Delta\eta$-gap). After background subtraction the distribution is integrated around the near- and away-side peaks, in the ± 0.7 and $\pi \pm 0.7$ $\Delta\varphi$ intervals, respectively. The per-trigger yields of associated particles, obtained this way, are normalized to the same yields measured in pp collisions. Such a ratio is denoted I_{AA} and it represents the nuclear modification factor of the conditional yields. In Fig. 13 the near- and away-side I_{AA} are presented as a function of associated-particle p_T^a for peripheral and central Pb–Pb collisions. The results are practically independent on p_T^a, and for peripheral collisions compatible with unity, i.e. no nuclear modification is observed. For central collisions, the away-side I_{AA} is around 0.6, which is interpreted as a manifestation of jet quenching. On the near-side the I_{AA} is above unity, such an effect was not observed at lower energies. The near-side enhancement could be understood as due to a modification of the fragmentation function, possibly caused by jet quenching and a trigger bias. This measurement constrains various models, some of those showed to be capable to describe such an enhancement.

The jet-shape studies measuring the jet-structure widths in $\Delta\varphi$ and $\Delta\eta$ directions, exploited the triggered two-particle correlations as well. It was reported that the $\Delta\eta$ jet-structure size increases for more central Pb–Pb collisions, while in the $\Delta\varphi$ direction such an increase, if any, is much smaller. This could be explained by an interaction of the jet with longitudinally flowing medium. The particle composition of the jet-like structure was also studied. The p/π ratio is measured in $(\Delta\varphi, \Delta\eta)$ regions, both outside and inside the jet structures selected in the correlation plot. Correcting the jet region with properly weighted outside-jet measurement, the p/π ratio for the jet structure is obtained. While
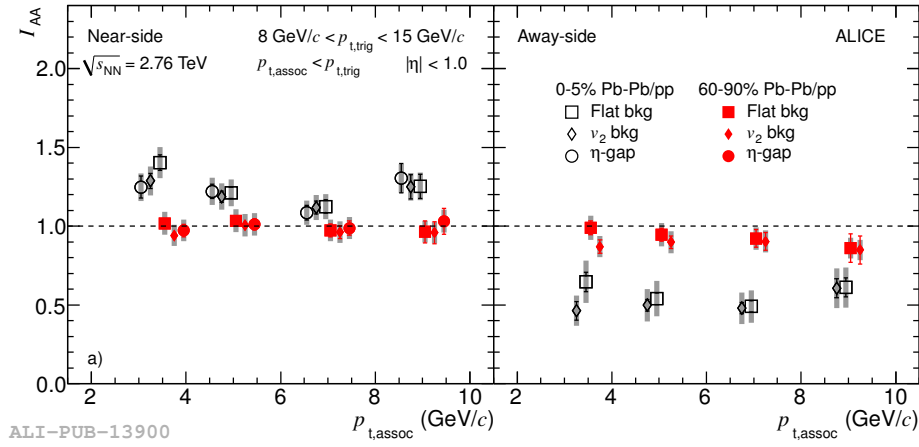
Figure 13: Near-side (left) and away-side (right) I_{AA} as a function of the transverse momentum of associated particles. The results are shown for peripheral (60–90 %) and central (0–5 %) Pb–Pb collisions. The three values shown for each measurement correspond to the three background subtraction methods described in the text. Reproduced from [].

the outside-jet p/π ratio reproduces the heavy-ion baryon anomaly (see Sec. 3.2), the result for the jet structure is compatible with the expectation for the jet fragmentation in pp collisions.

The study of the charge balance function is performed using the correlations constructed for unlike-sign and like-sign particle pairs separately. The balance function is defined as one half of the difference between the unlike-sign and like-sign correlations, and measures the distance over which the charge of particles is compensated. The widths of the balance function in the two directions, $\langle \Delta\varphi \rangle$ and $\langle \Delta\eta \rangle$, are shown in Fig. 14 as a function of the collision centrality. The measurement indicates that the charge is compensated in both directions on a shorter scale for more central collisions. Such behaviour was already observed at RHIC, however, the $\langle \Delta\varphi \rangle$ and $\langle \Delta\eta \rangle$ values are significantly larger at the LHC. The model calculations presented in Fig. 14 have difficulties to reproduce the centrality dependencies in both directions.

5 Flow correlations

5.1 Introduction

While the previous section covered physical mechanisms which induce correlations between multiple hadrons, this section covers the phenomenon of "collective flow", which leads to the correlations of essentially all the particles in every event. This results from the translation of anisotropies in the initial shape of the colliding nuclei into anisotropies in momentum space, something that would not occur if individual nucleon-nucleon collisions emitted independently of each other. The characterization of a "shape" in a final state particle distribution is typically performed using a Fourier decomposition of the azimuthual angle distrbution of final state particles. Of course, averaging over an ensemble of independent events would lead to the observation of no net anisotropy. Thus, the presence of harmonic oscillations in the final state requires the estimation of an "event plane" from the particle themselves, with an axis that points in the direction of the largest momentum flow.

While this phenomenon was observed decades ago in the collisions of large nuclei at low energies, this was straightforward to understand as the reinteraction of the initial baryons and the produced hadrons, which would thermalize and evolve as a "hadron gas". However, its persistence at higher energies, particularly at RHIC where the value of v_2 averaged over p_T was twice as large as it was at the CERN
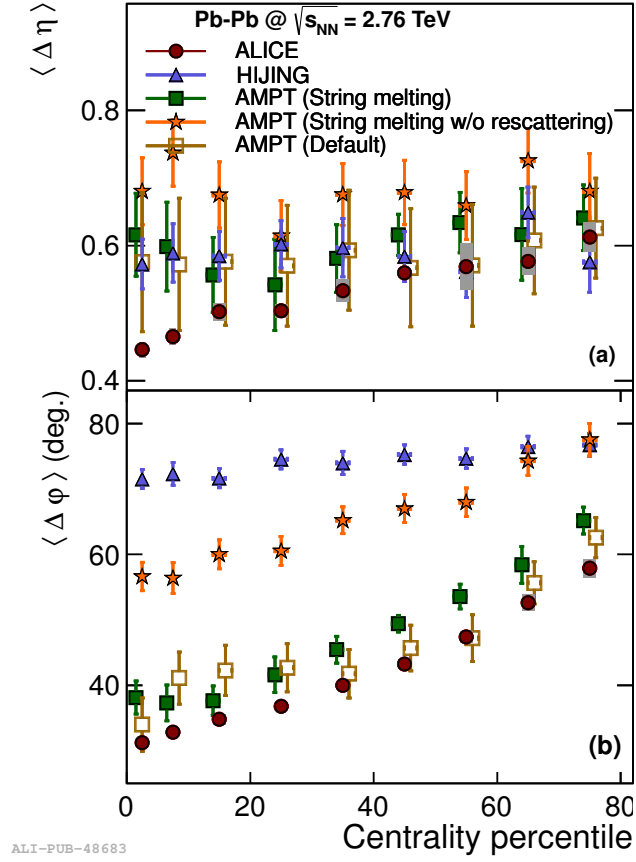
20

Figure 14: Charge balance function widths in longitudinal (upper part - a) and azimuthal (lower part - b) directions as a function of collision centrality, expressed in percentiles. Model calculations are presented with markers according the legend. Reproduced from [].

SPS, surprised many who expected the hot system to become more dilute and more weakly-interacting at higher energies.

Collective flow was a major piece of the RHIC program, and its characterization in terms of hydrodynamics was a crucial piece of evidence in the RHIC discovery of the strongly-coupled quark gluon plasma (sQGP). Crucial aspects of collective flow, on the experimental and theoretical sides at RHIC, have been:

- Based on theoretical calculations, the average elliptic flow, scaled by the eccentricity, is thought to reach a limiting value in the limit where the viscosity can be ignored. RHIC data achieved this limit both integrally (integrated over p_T) and for $v_2(p_T)$, which rises linearly until viscous corrections become large.

- When studied as a function of particle type, it is found that heavier particles show a smaller v_2 at the same p_T at low p_T, while this hierarchy flips above 1.5 GeV, where protons typically have a 50% higher value of v_2. This behavior has been explained by the hadronization of the system via constituent quarks which recombine into baryons with $v_2(\text{baryon})=(3/2) \times v_2(\text{meson})$.

- The deviations from ideal behavior can be systematically calculated by viscous corrections, and all RHIC data point to a small but significant value of the ratio of shear viscosity to entropy density (η/s).

- While difficult to calculate in the strongly-coupled limit, where the approximations required for kinetic theory break down, AdS/CFT-based calculations have shown that a wide range of strongly-coupled systems have a lower-bound on $\eta/s = 1/4\pi$. The RHIC experimental data suggest values of 1-2 times this bound, although esimates are limited by theoretical uncertainties related to the modeling of the initial state.

- When studying smaller systems (particularly Cu+Cu), it was found that accounting for the event-by-event position of the nucleons in the nuclear wave functions showed scaling in the quantity v_2/ϵ between Cu+Cu and Au+Au, when plotted as a function of the transverse density of charged particles at mid-rapidity, estimated by $dN_{ch}/d\eta/S$, where S is the overlap area of the two nuclei.

5.2 Methods

Harmonic flow is a global modulation of essentially all of the particles in an event relative to an event plane appropriate to each harmonic. However, there are additional sources of multiparticle correlations, some which lead to global correlations (momentum conservation) and others which only lead to correlations local in angular space (e.g. resonance decays and jets). Thus, care must be taken to minimize such "non flow" correlations.

One of the earliest methods for measuring flow was the "event plane" method, which calculates an event plane using a forward detector and correlates all particles with this event plane, based on the so-called "Q-vector" for each order n:

$$(3)$$

From this, the n-th order event plane Ψ_n is simply determined as the angle of the Q-vector itself. From the definition of the Q-vector, the angle is n-fold ambiguous, but this has no effect on the extracted v_n coefficient, which is defined as

$$v_n = \frac{v_n^{obs}}{/}\text{Res}\{n\Psi_n\} = \frac{\langle\cos(n[\phi - \Psi_n])\rangle}{\langle\cos(n[\Phi_n - \Psi_n])\rangle} \tag{4}$$

where Φ_n is the direction of the true event plane. The latter quantity cannot be observed directly and so the resolution parameter must be derived from comparison of different detector regions. This is typically done by comparing symmetric pseudorapidity regions separated from the region being measured:

$$\text{Res}\{n\Psi_n^{P(N)}\} = \langle \cos n(\Psi_n^{P(N)} - \Psi_n) \rangle = \sqrt{\langle \cos n(\Psi_n^P - \Psi_n^N) \rangle} \qquad (5)$$

Non-flow contamination is typically most difficult to control when the subevents used to determine the event plane and resolution are close in η to each other or close to the measured particles. Another method is to use multiparticle cumulants to explicitly remove lower order correlations. These can be calculated either from a generating function formalism, or through moments of the Q-vector itself. They are more or less sensitive to non-flow depending on the order of the cumulant. For example, the two-particle cumulant is quite senstitive to effects from resonance decay and jet fragmentation. However, the four particle cumulants are generally much less so, since it explicitly removes short-range two particle correlations. A third method is to use the "Lee Yang zeroes" approach, which accounts for correlations of all lower orders using a different generating function. The method relates the zeros of a complex function to the magnitude of the relevant flow harmonics. While the method is thought to be robust against most sources of non-flow, it is particularly sensitive to multiplicity fluctuations, and so is calculated using event samples with similar multiplicities within a given centrality interval. Theses subsamples are then averged within the desired centrality interval to give the final result.
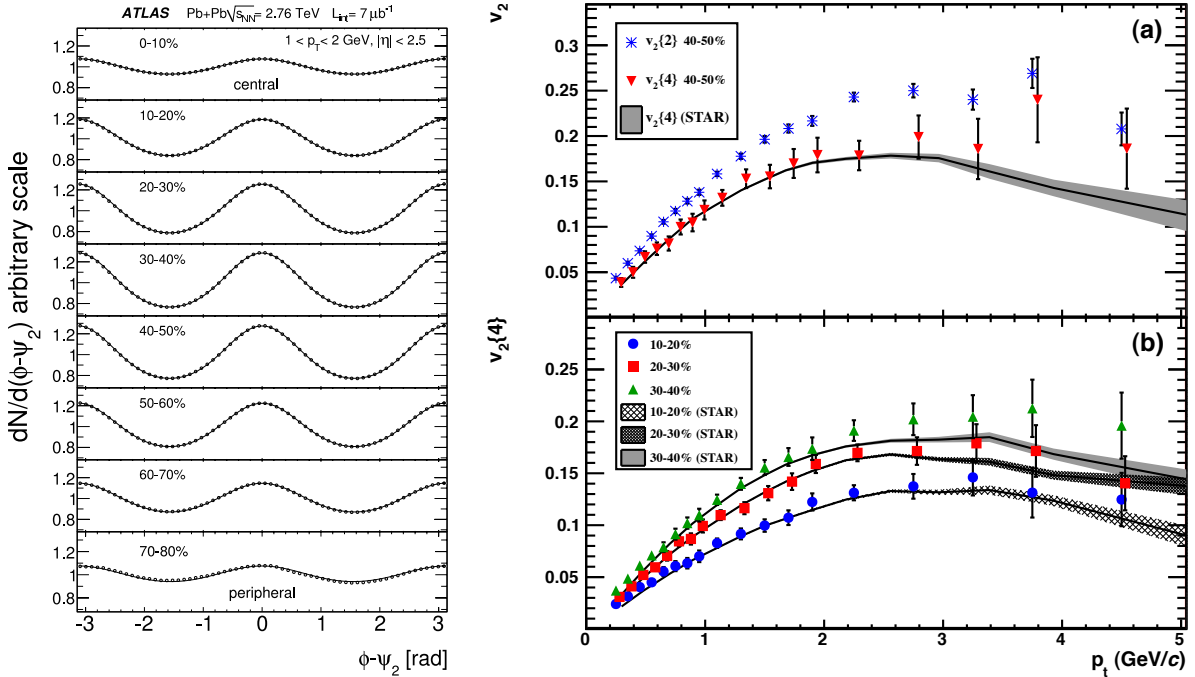
5.3 Elliptic flow

Figure 15: (left) ATLAS data showing the evolution of anisotropy relative to the reaction plane, as a function of centrality [?] (right) First ALICE data on v_2 in Pb+Pb collisions at the LHC [?].

The first LHC data on elliptic flow was released by the ALICE collaboration soon after the first collisions, and is shown in Figure ??. The elliptic flow was estimated using three methods: 2-particle cumulants ($v_2 2$), 4-particle cumulants ($v_2 4$) and Lee-Yang Zeros (LYZ). The first method is known to be sensitive to correlation from jets, which have a larger contribution at the LHC than at RHIC, and

the latter method was only used for integral flow. The integral flow was found to be larger than that measured at RHIC, but only by about 15-20%. What was surprising was that, as a function of p_T (but only measured out to 4 GeV) the magnitude of v_2 was found to be quantitatively very similar to that measured in the STAR experiment at RHIC, using similar cumulant methods. Although a similar scaling has been observed in the very low energy data on inclusive $v_2(p_T)$ from STAR taken during the recent RHIC energy scan, there is no fundamental understanding yet of how this scaling arises. It suggests that most of the variation in the integral elliptic flow results from the change in the spectral shape of inclusive hadrons. Hydrodynamic calculations were able to reproduce this result, soon after its release, estimating a slightly higher viscosity to entropy ratio based on a scaling of the initial energy density according to the measured charged-particle multiplicity [**?**] [CHECKME]. The first v_2 measurement at higher p_T was performed by ATLAS [**?**], showing the transition from the low p_T behavior, understood by viscous hydrodynamics, to the higher p_T values presumably explained by the path-length dependence of energy loss of jets. By comparison with PHENIX data on π^0 particles, this shows that the scaling of v_2 extends to high p_T as well, within the large statistical errors of the lower-energy measurement.
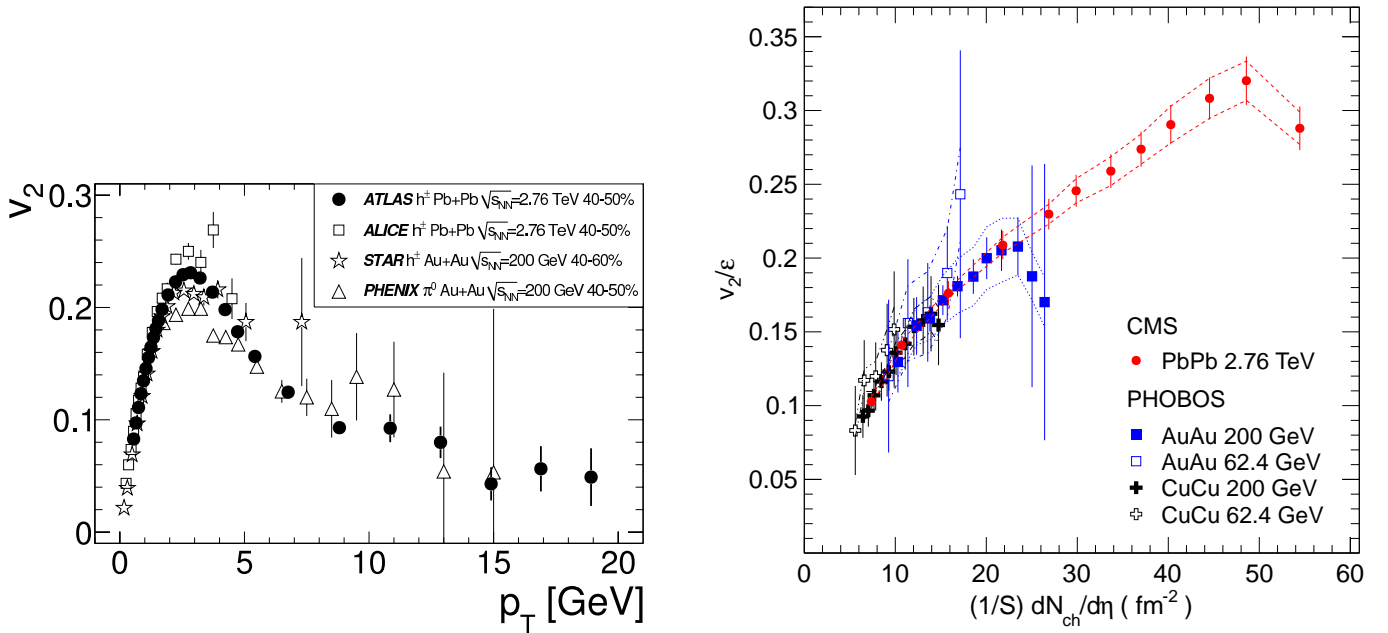

Figure 16: (left) ATLAS data showing the invariance of $v_2(p_T)$ with beam energy [**?**] (right) CMS compilation showing the observed scaling of v_2/ϵ vs. $(1/S)dN_{ch}/d\eta$ [**?**].

The dependence of the inclusive elliptic flow on the initial state geometry was studied carefully by CMS, who performed a careful extrapolation of the integral v_2 down to $p_T > 0$ GeV, using simultaneous measurements of dN/dp_T, to match with the lower energy PHOBOS data. To factor out the initial shape and size of the overlap region, a Monte Carlo Glauber model was used to match the centrality selections made with the CMS forward calorimeter. From these, the eccentricity and overlap area were calculated according to the definitions from subsection **??**. The CMS data, shown superimposed on data from RHIC, is shown in Figure 16(right), and overlaps the PHOBOS data in the most peripheral collisions and shows a continuous rise in the more central collisions, except perhaps in the most central interval.

The CMS data shown in Figure 17 illustrates the p_T and centrality dependence of $v_2(p_T)$, comparing directly the different methods of flow reconstruction used for v_2. While it is clear that the 2-particle cumulant is the most contaminated by non-flow, particularly at high p_T, one also observes some systematic
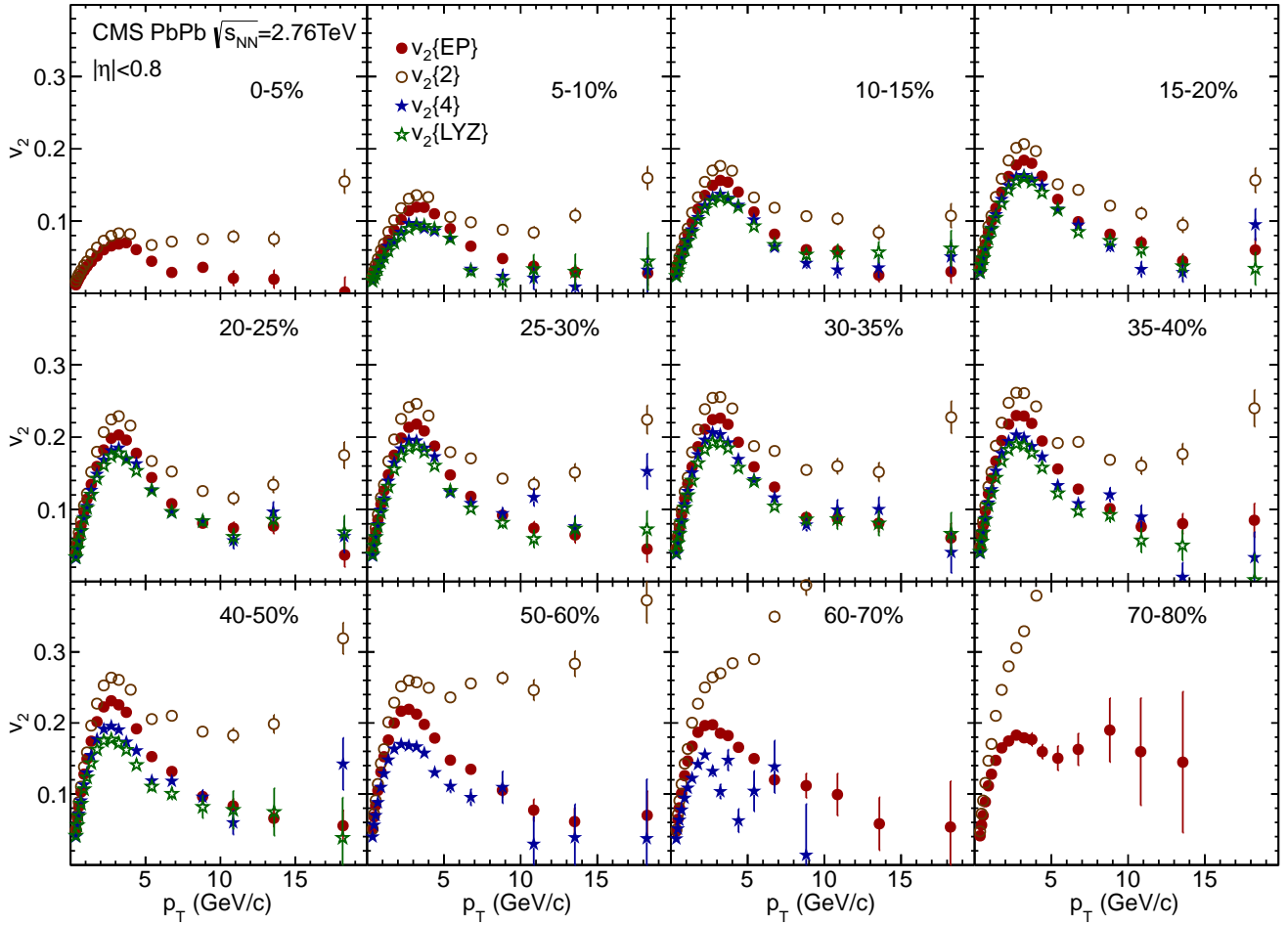
Figure 17: CMS data showing $v_2(p_T)$ in centrality intervals, using four different methods of extracting v_2: event plane (EP), 2-particle cumulants, 4-particle cumulants, and Lee-Yang Zeros [**?**].

differences between all three methods, particularly where the flow is the strongest.

The previous results have all been for unidentified hadrons. This choice provides the largest phase space coverage (particularly in p_T) and allows for comparisons between experiments with different particle identification capabilities. However, a study separating the different hadron species is crucial, given the previous measurements at RHIC showing the strong differences between them. The ALICE data showing identified particles (separated using the dE/dx measured in the ALICE TPC) for $p_T > 3$ GeV is shown in Figure 18(left). The charged pion data on $v_2(p_T)$ is quantitatively similar to the PHENIX π^0 data over the p_T range where they overlap. The proton-antiproton v_2 are found to be subsantially larger than the pion values over the measured p_T range, although it is clear that the peak-plateau structure seen in the inclusive hadron data is not explained primarily by one particular hadron type. Also, at the highest p_T measured, the protons and pions are quite close, although the protons remain systematically higher out to 14 GeV. CMS extends the hadron p_T range out to the full range provided by the LHC in 2011, using a high p_T high level track trigger. The data, shown in Figure 18(right), show that the plateau observed setting in above 6 GeV extends out to 50 GeV, with only mild decreases observed within the stated uncertainties.

Another intriguing way to compare with the lower energy data is suggested by studies performed by the PHOBOS collaboration, which found that the integrated $v_2(\eta)$ is the same for different colliding
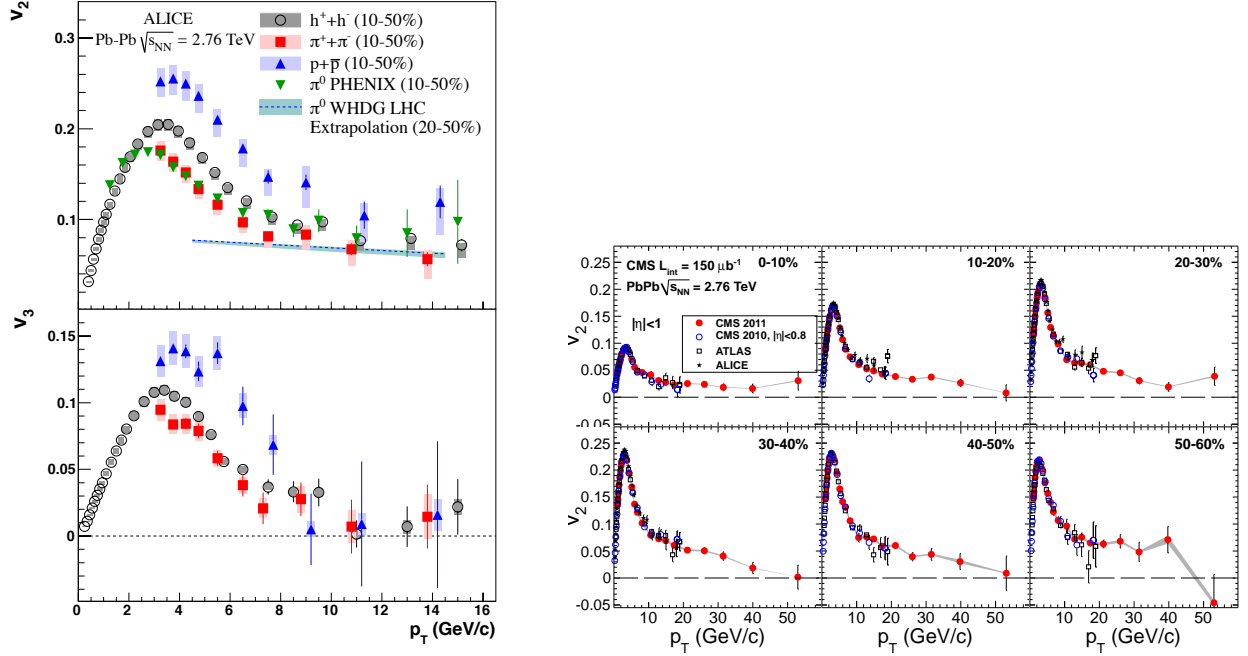
Figure 18: (left) ALICE data showing $v_2(p_T)$ for identified hadrons, for $|\eta| < 0.8$ [?] (right) CMS data showing the v_2 for unidentified hadrons at very high p_T, out to 50 GeV [?]
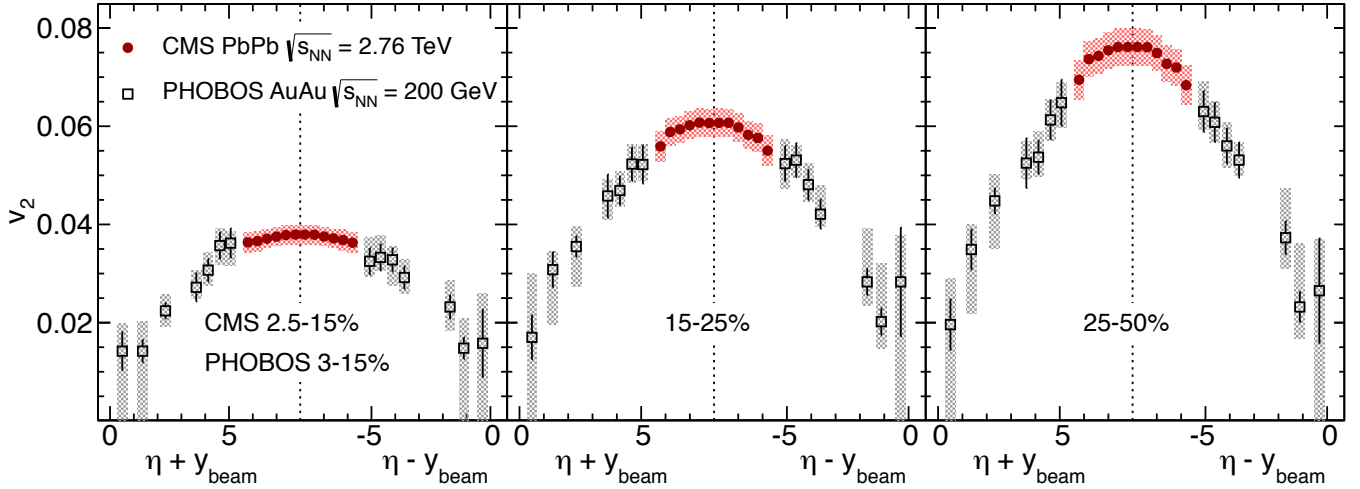

Figure 19: CMS data showing v_2 for unidentified hadrons as a function of $\eta - y_{\text{beam}}$, averaged over $0 < p_T < 3$ GeV (using an extrapolation procedure to cover $p_T < 300$ Mev). Results are compared to data from $\sqrt{s_{NN}} = 200$ GeV at large η from the PHOBOS experiment at RHIC [?].

beam energies, when plotted in the rest frame of one of the projectiles. This is the phenomenon of so-called "limiting fragmentation", where many quantities are found to depend only on their rapidity relative to either beam or projectile. Figure 19 shows $v_2(\eta)$ as a function of $\eta - y_{\text{beam}}$ (in the forward hemisphere) and $\eta + y_{\text{beam}}$ in the backward hemisphere. While the CMS and PHOBOS data points do not overlap in any measured region, they appear to be continuous in the forward LHC kinematics and the mid-rapidity RHIC kinematics. However, it is clear that the behavior of the CMS data is much

more suggestive of a boost-invariant central plateau, while the PHOBOS data did not show similar behavior.
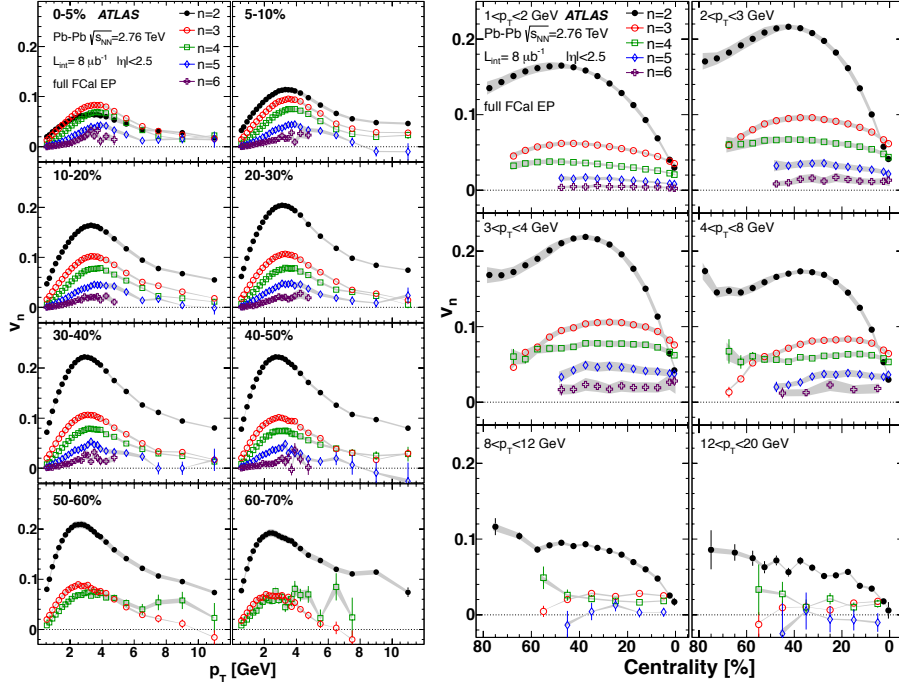
5.4 Higher order harmonics

Figure 20: (left) ATLAS data showing $v_n(p_T)$ for different centrality intervals and $|\eta| < 2.5$, for $n = 2-6$. Very little dependence on η is observed [?]. (right) The same ATLAS data, in p_T intervals, showing the centrality dependence of v_n [?].

Although the realization that v_2 was sensitive to fluctuations in the nuclear overlap, particularly from the eventwise random positions of nucleons in each nuclei, several more years elapsed before it was suggested to look for higher-order harmonic flow, particuarly odd-orders [?]. Many authors argued that symmetric systems would have a zero v_1, v_3, v_5, etc, but had not yet considered the effect of fluctuations. By mid-2011, all of the LHC and RHIC experiments had significant measureents of many of the higher-order contributions, up to v_6 which was the limit of the statistics in the 2010 run.

CMS released the first evidence for the presence of higher-order harmonics in the two-particle correlation function. ALICE released the first measurements of of $v_3 - v_5$ up to $p_T = 4$ GeV, using two and four particle cumulants [?], and followed up with an extensive study of two-particle correlations in Ref. [?]. ATLAS released the first large scale study of higher harmonics for unidentified hadrons, with the first complete experimental measurements of

The ATLAS data shown in Figure 20(left) and (right) show the harmonics $v_2 - v_6$ as a function of p_T in centrality intervals from the most central 0-5% to the most peripheral 70-80%. The the figure on the left shows that the pattern is consistently the same for all harmonics: a rapid rise starting at low p_T, a peak around 3 GeV, and a rapid decrease out to higher p_T. While all of the experiments have demonstrated that v_2 does not necessarily go to zero at high p_T, it remains an open question about the higher harmonics, which can only be resolved with higher statistics. The right figure shows the centrality dependence in small p_T intervals, demonstrating that v_2 is fundamentally different than the higher harmonics, having a much milder centrality dependence. While v_2 mainly reflects the overall

geometric shape of the system, the higher harmonics seem to mainly reflect fluctuations. However, the decrease in magnitude with increasing n is generally thought to reflect the presence of viscous effects.
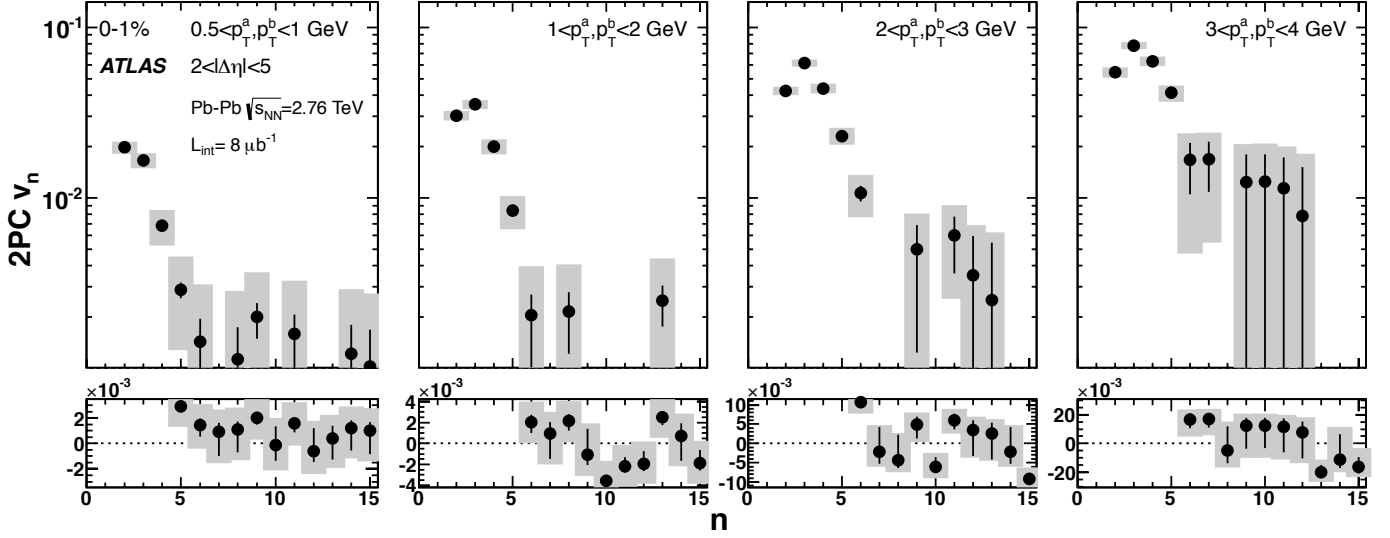

Figure 21: ATLAS data showing the n dependence of v_n in four p_T intervals, which are effectively angular power spectra at different resolution scales.

Another representation of this data is given in Figure 21, which shows the "angular power spectrum", the n dependence of $v_2(p_T)$ for particular intervals in p_T and centrality. The fall-off with increasing n is a general feature, of the data which is expected to be driven by viscous corrections that increase with n.

While the two-particle analyses from ALICE, ATLAS and CMS all utilized a $v_{1,1}$ term in their fits, the first measurements did not extract a single-particle v_1 contribution, since momentum conservation is expected to be a substantial effect. The first published extraction of v_1 from experimental data was performed by a theoretical team using published ALICE data, doing a fit of the form $V_{1\Delta}(p_T^a, p_T^b) = v_1(p_T^a)v_1(p_T^b) - kp_T^a p_T^b$. ATLAS was the first experimental group to measure directed flow from its own data, using the same approach as Ref. [?](but performed in isolation from it), fitting $v_1(p_T)$ The value of v_1 was also found to change very little with centrality, suggesting it too arises from fluctuations.

5.5   Flow fluctuations

The same geometric fluctuations that lead to the presence of the higher harmonics are also expected to lead to event-by-event fluctuations in the individual coefficents. This has been studied using two methods. ATLAS developed a data-driven method to unfold the measured v_n distributions ($P(v_n)$) with a Bayesian technique. The distributions $P(v_n)$ are shown in Figure 23 for v_2, v_3 and v_4 for a selected set of centrality intervals. It is clear that the fluctuations are large in all selected samples. Although the distributions are not Gaussian, but are rather projections of a 2D Gaussian (also known as a Bessel-Gaussian distribution), the distributions are typically quantified using the first two moments, the mean and standard deviation. These can also be estimated by combining different estimates of v_n, in particular using the event-plane and 4-particle cumulant methods. Based on the analysis of Ref., the difference between these quantities is twice the variance, while their sum is twice the squared mean. Figure 24(left) shows CMS data on $\sigma/\langle v_2 \rangle$ derived from cumulants, compared with the ATLAS data derived from the fully unfolded distributions. While the v_2 fluctuations compare well between the two methods, the ATLAS and CMS results on v_3 are quite different, possibly from the inapplicability of
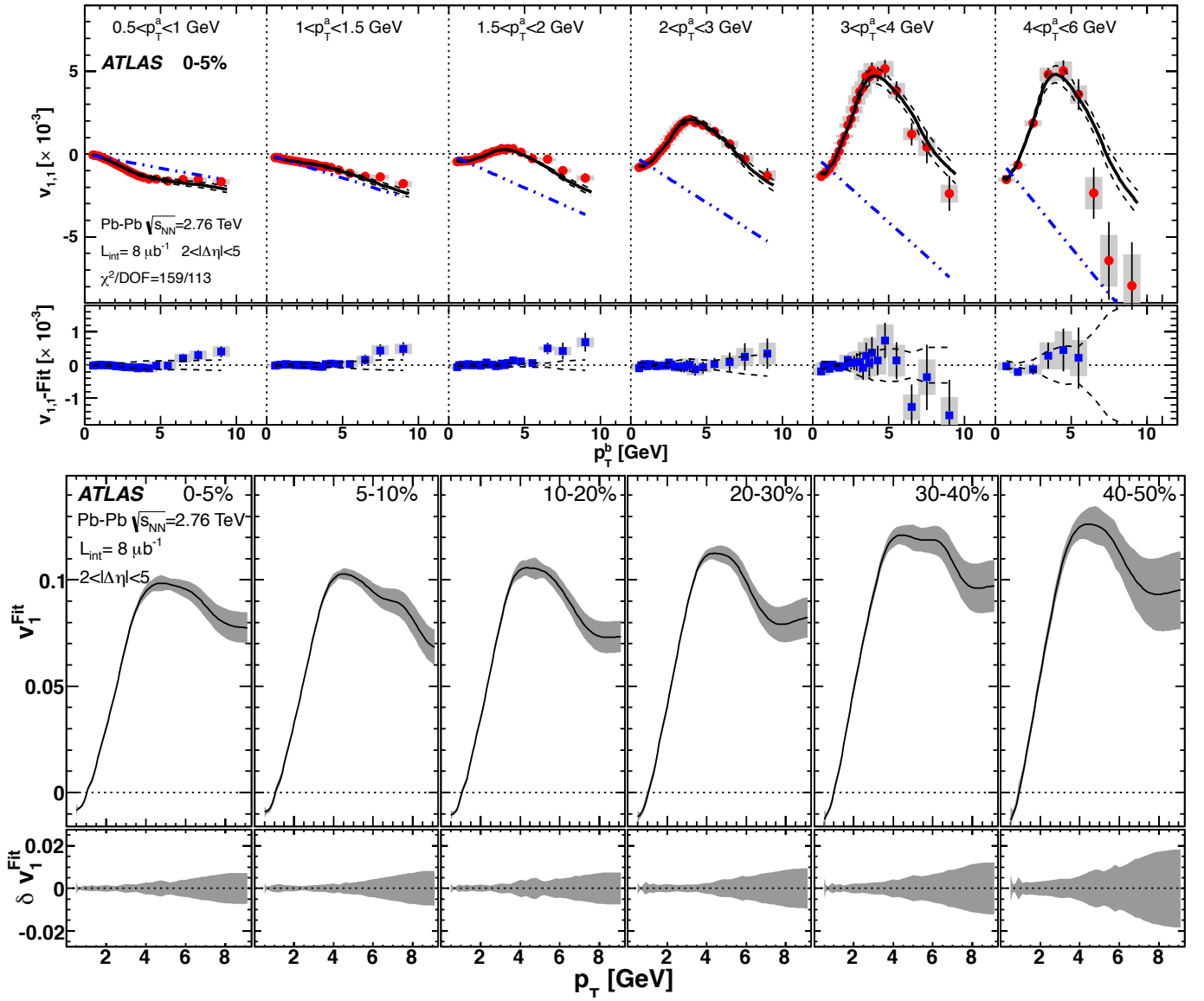
28

Figure 22: (top) ATLAS data showing the amplitude of $v_{1,1}$ the dipole modulation in the 2-particle correlation function, as a function of p_T^b for ranges in p_T^a. The fit used to extract the functional form of $v_1(p_T)$ is shown [?]. (bottom) The extracted functional form of $v_1(p_T)$, from the fits shown above, as a function of centrality [?].

the cumulant approach for this quantity. The ATLAS results are essentially constant for all centrality intervals at around 0.5, which is the value one gets ($\sqrt{4/\pi - 1}$) if the fluctuations are described by a 2D Gaussian, projected along the radial direction. Figure 23(left) shows ALICE data on $\sigma/\langle v_2 \rangle$ derived using a similar approach as CMS. For centrality intervals from 5-60%, the overall magnitude is similar to that seen by the other experiments. However, this figure points out that the fluctuations have essentially no centrality dependence out to moderately large p_T, about 8 GeV, which reaches into the plateau region typically associated with differential energy loss.
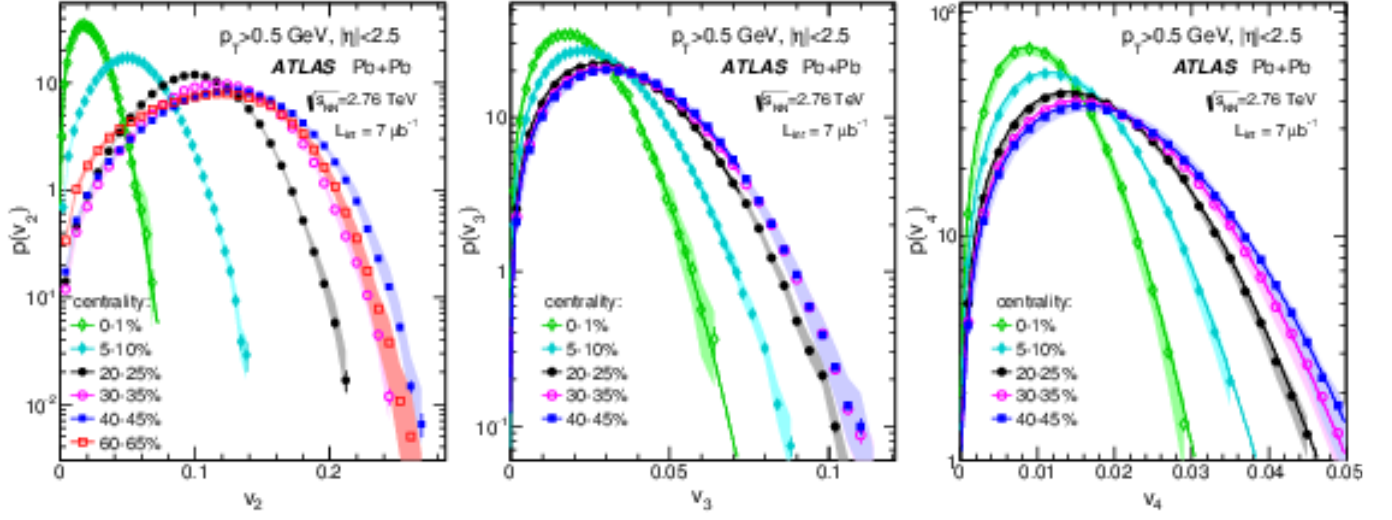
Figure 23: ATLAS data on the event-wise distributions of the harmonic coefficients $v_2 - v_4$ presented in a selection of centrality intervals, from Ref. [?].
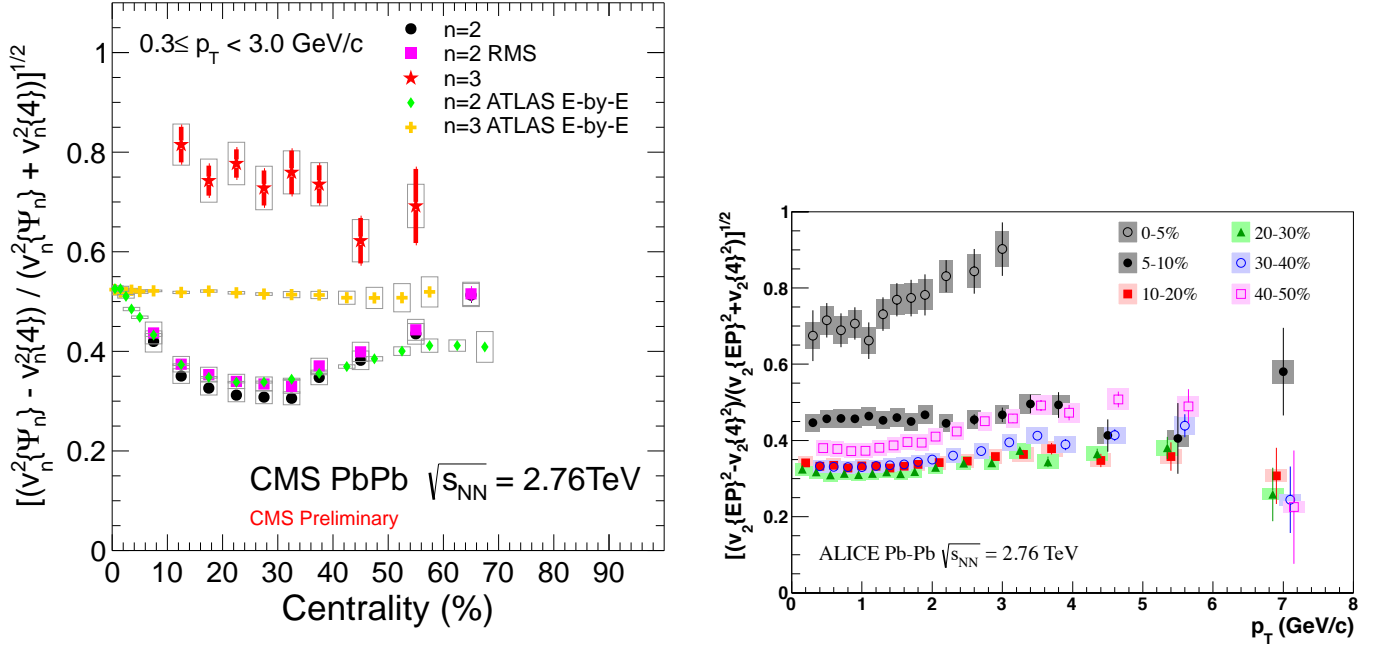

Figure 24: (left) CMS data on the centrality dependence of the standard deviation of v_2 divided by the mean, for $0.3 < p_T < 3$ GeV, extracted via the differences between the EP and cumulant results [?]. (right) ALICE data on the p_T dependence of the same quantity, out to $p_T = 8$ GeV, for a selected set of centrality intervals [?].

6 Electroweak probes

While a primary topic in the study of heavy ion collisions is the modification of jets in the hot and dense nuclear medium, typical analyses of hard processes have assumed that the structure of a nucleon in a nucleus-nucleus collision is quantitatively the same as one in a nucleon-nucleon collision. From analyses of lepton-nucleus deep inelastic scattering data, it is known that cross sections do not scale linearly with

the number of nucleons, as might be expected simply from the availability of scattering centers. The deviations from this scaling are referred to generally as "nuclear shadowing", and are typically shown as a function of Bjorken x for different ranges in the hardness scale Q^2. The region around $x \sim 0.1$ corresponds to the valence quark region for a standard nucleon, and this is usually enhanced. The region above this, $x \geq 0.2$ is typically suppressed (the so-called "EMC effect"), while the region below $x << 0.1$ is also suppressed down to very small values of x. The latter phenomenon is more typically known as "nuclear shadowing" and is thought to arise generally from quantum mechanical effects which deplete the numbers with small fractions of the nucleon momentum.

It is important to understand the magnitude of these sorts of effects in the realistic environment of a heavy ion collision, in order to properly interpret measurements of hard process rates relative to a nucleon-nucleon reference system. At the RHIC collider, this was addressed early in the experimental program through measurements of high p_T particles in deuteron-gold collisions. Presumably, any gross effects related to modifications of nucleon structure in the nuclear environment would show up as modifications in this system. It was found that hadrons above ~ 2 GeV were produced at expected rates near $\eta = 0$, confirming that the high p_T suppression observed in the early days of the RHIC program did not arise from changes in nucleon structure, and strengthening the case for jet suppression in the hot and dense medium. However, it was also found that hadrons and J/ψ particles were suppressed at forward angles, in the direction of the incoming deuteron, especially in more "central" d+Au collisions, and enhanced slightly at backwards angles, in the direction of the nucleus. These features are in broad agreement with predictions from calculations incorporating the nuclear shadowing observed in lepton-nucleus DIS.

While the measurement of hadronic final states in proton (or deuteron)-nucleus collisions is thought to give useful information on modifications in the initial state of these simpler systems, the abovementioned observed modifications of jets precludes similar observables giving similar information in heavy ion collisions. For this reason, great attention has been given to the measurement of "penetrating probes", particles which do not interact strongly after they are produced. While charged leptons and neutral photons, of course, do not interact strongly, they come predominantly from jets and hadrons at relative low $p_\mathrm{T} < 20$ GeV. However, at high p_T, most leptons are known to arise from the decay of electroweak bosons (Z and W particles). Furthermore, isolated photons at high p_T are predominantly "prompt", i.e. arising from the direct interactions of quarks and gluons and not from electromagnetic decays of hadrons (π^0 and η).

While the production cross sections for the heavy bosons are prohibitively small at the top RHIC energies (200 GeV per nucleon-nucleon collision), the LHC provides the first heavy ion system where all of the electroweak bosons are produced at substantial rates. This section presents measurements of all three particles in Pb+Pb collisions at the LHC, and shows their comparisons either with nucleon-nucleon reference data, or cross sections calculated with perturbative QCD using standard structure functions. The main physics goals of these measurements are twofold

- To establish whether the production of the vector bosons is proportional to the nuclear thickness or, equivalently, the number of binary nucleon-nucleon collisions

- To see whether any modifications of vector boson production can be observed, and if they can be attributed to modifications of the nuclear PDFs

Theoretical calculations provide some guidance as to the magnitude of the modifications of standard PDFs expected in nPDFs, but substantial uncertainties remain due to the different parametrizations of the existing nDIS data. One feature which is predicted generically, however, is the decreasing magnitude of nuclear modifications with increasing Q^2. As shown in Fig., the large magnitude of shadowing expected at low Q^2 (i.e. low p_T) is reduced substantially even by $Q^2 = 100$ GeV. Thus, the large values of M_Z and M_W are already 80-90 GeV, naturally lead to nuclear modifications only at the 10-15% level.

Figure 25: (left) Modifications to proton PDFs expected from different nPDF implementations, for $Q^2 = 1.69$ GeV^2, (right) Modifications to proton PDFs expected from different nPDF implementations, for $Q^2 = 100$ GeV^2 from Ref. **??**.

6.1 Measurements of W and Z bosons in Pb+Pb collisions

The first observation of vector bosons in Pb+Pb collision was performed by the ATLAS experiment with a set of 38 Z candidates obtained in the first heavy ion run in 2010, which was followed several months later by a CMS result comparing with theoretical calculations. However, the statistical power of the 2010 sample was not sufficient to make strong conclusions about the Z production rates as a function of the nuclear thickness. The situation has improved dramatically with a published measurement of W bosons by CMS, also from the 2010 dataset, but benefiting from the large increase in the W cross section compared with Z. ATLAS has also published the yield and spectrum of Z bosons from the much larger 2011 Pb+Pb dataset. Together these give a relatively complete first look at the behavior of heavy vector bosons in heavy ion collisions.
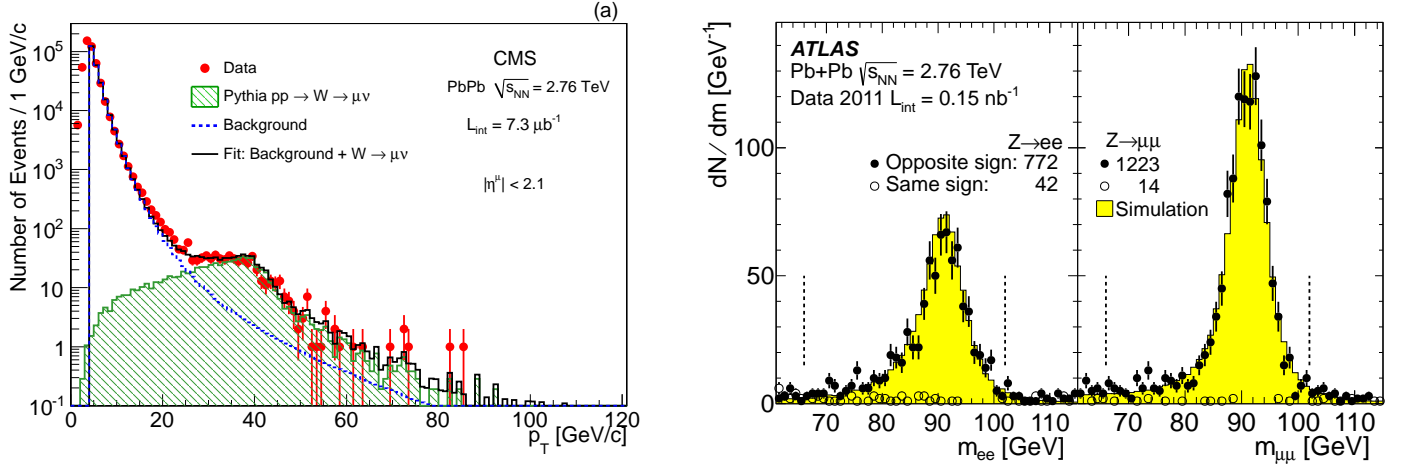

Figure 26: (left) Single muon spectrum, after selection cuts, from CMS data [**?**] (right) Dimuon mass spectrum, in electron and muon channels from ATLAS data [**?**].

The CMS W measurement was performed using the CMS inner tracker, which covers $|\eta| < 2.4$ and the CMS muon spectrometer, which covers $|\eta| < 2.4$ using a variety of gaseous detectors (CSC, DT, with RPCs used for triggering), but was restricted to $|\eta| < 2.1$ in this particular analysis. The ATLAS Z measurement was performed combining dilepton decays in the muon and electron channels. The ATLAS muon spectrometer uses drift tubes and cathode strip chambers to measure muons with $|\eta| < 2.7$ in tandem with the ATLAS inner detector covering $|\eta| < 2.5$. Electrons are measured in ATLAS using the inner detector in association with the ATLAS calorimeter system, which is particularly finely segmented in η for $|\eta| < 2.5$, allowing rejection of jet backgrounds.

As shown in Figure 26(left) from CMS, the single muon spectrum at high p_T clearly shows a contribution from W bosons as a peak near 40 GeV. The backgrounds from jets are strongly reduced by calculating the missing p_T for each event with a high p_T muon, based on tracks with $p_T > 3$ GeV. The background from Z bosons is removed by removing muons which combine with a second muon in the same event that reconstructs to a mass near the Z mass. After selections, about 540 W candidates were found in the 2010 Pb+Pb data. Figure 26(right) shows the dimuon and dielectron mass spectrum after

requiring $p_T > 10$ GeV for the muons, and $p_T > 20$ GeV for the electrons. The Z lineshape is in good agreement with simulations for both dielectron and dimuon channels. After selections, about 2000 Z candidates were reconstructed in the 2011 Pb+Pb data.
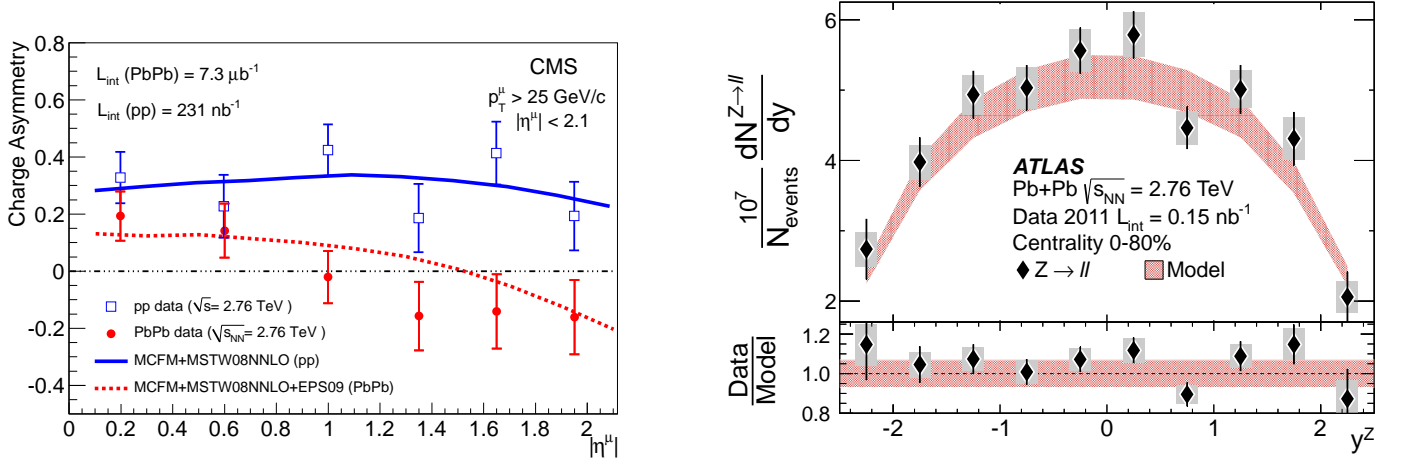

Figure 27: (left) Charge asymmetry for W candidates, from CMS data [?] (right) Rapidity dependence of dN_Z/dy compared to PYTHIA scaled to the NNLO cross section [?]

Figure 27(left) shows the pseudorapidity dependence of the charged lepton asymmetry for the muons associated with W candidates ($A_\mu = (N_{W^+} - N_{W^-})/(N_{W^+} + N_{W^-})$), both for Pb+Pb and p+p data at the same CM energy ($\sqrt{s_{NN}} = 2.76$ TeV). The evident differences between the Pb+Pb and p+p stem primarily from the neutrons in the Pb nuclei, which modify the expected charge distribution, particularly in the forward direction where the Bjorken x probed is sensitive to the valence quarks. Both data sets are compared with NNLO calculations of the W charge asymmetry and good agreement is found for both p+p and Pb+Pb. While this suggests that no large nPDF effects are needed to accomodate the existing data, it was pointed out in Ref. ?? that the scale factors in EPS09 formalism will cancel out in the charge asymmetry ratio, making this quantity suboptimal for isolating nPDF modifications.

Figure 27(right) shows the rapidity dependence of the per-event Z boson yield in the 0-80% centrality interval in Pb+Pb collisions from the 2011 ATLAS Pb+Pb data. The data is compared to the same distribution from PYTHIA (version 6.425), scaled to the NNLO total cross section, and the appropriate mean nuclear thickness. Good agreement is found between the heavy ion data and the absolutely-scaled PYTHIA reference, the ratio between them being consistent with unity within the stated uncertainties. While small effects at the 10-15% level are not ruled out, nor are they required to make sense of the current measurements.

The centrality dependence of the separate W charge states and the total from CMS is shown in (left), as a function of the number of participating nucleons, and for the p+p data. While p+p shows a clear difference between positive and negative W's, reflecting the charges of the initial protons, there is little difference between them in the Pb+Pb data, reflecting the additional down quarks introduced via the neutrons in the Pb nuclei. The heavy ion data shows a clear scaling with centrality, once the W yields – both for the charge-separated yields, and the total – are scaled by the number of binary collisions. A similar message is found in the ATLAS Z data, shown in (right), which shows the Z yield, scaled by the number of binary collisions, also as a function of the number of the mean number of participating nucleons for each centrality interval. The ATLAS data also shows that the centrality dependence is the same for the dielectron and dimuon channels, and even for selected intervals in the Z p_T.
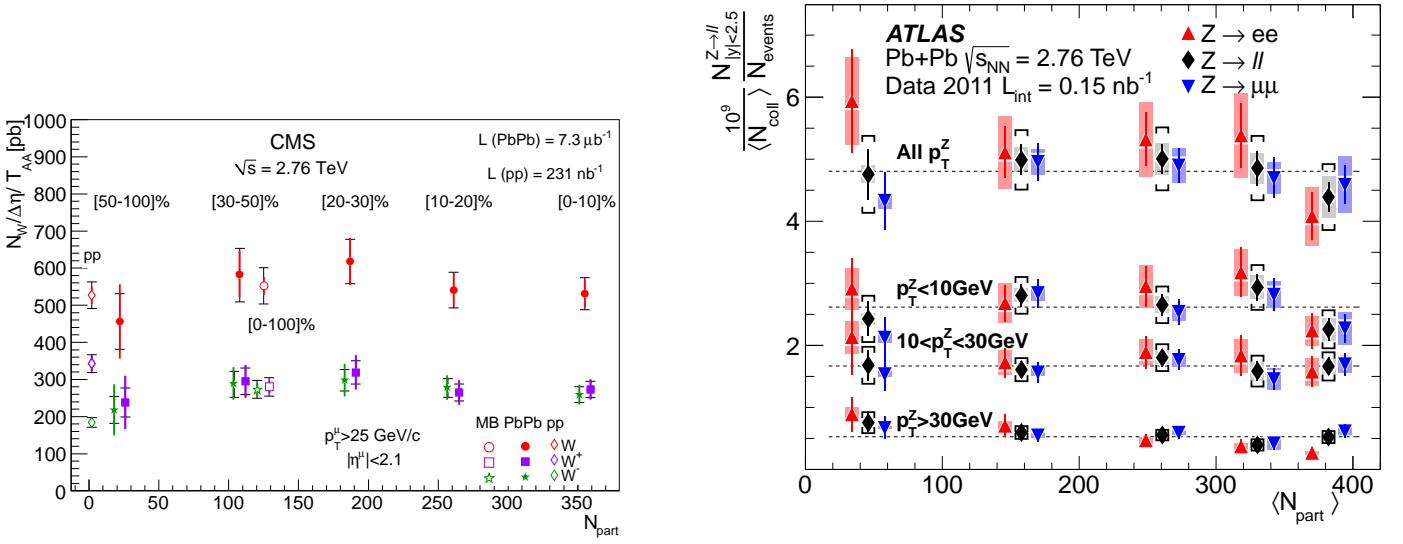
33

Figure 28: (left) Yield per collision for W candidates, from CMS data [?] (right) Yield per collision for Z's, in both electron and muon channels from ATLAS data. [?]

6.2 Measurement of isolated photons in Pb+Pb collisions

The measurement of photons in heavy ion collisions is also an important contribution to the study of the Pb+Pb initial state, with some advantages and disadvantages. Unlike Z and W bosons, no energy from the initial 2-to-2 scattering process is used in the boson mass, and so the cross sections at high p_T are substantially higher at the same transverse momentum. However, photon measurements do not provide a clear mass peak, and nor are they associated with a track measured in an inner tracker. This means that backgrounds are an irreducible part of the measurement, particularly at low p_T, where one expects large contribution from jet fragmentation into high momentum neutral pions or eta mesons.

Two primary techniques are used to increase the purity of the photon sample, which is typically $O(0.1\%)$ based on the expected relative yields of photons and jets. The first is to select photon candidates as electromagnetic clusters which pass a set of selection criteria, trained on photon simulations to efficiently reject electromagnetic decays while keeping most of the produced photons. These criteria involve both the "shape" of the cluster (since photon showers are typically quite narrow), as well as the presence of energy in the "hadronic" section of the experimental caloriemters (since photon showers should typically be well-contained in the front electromagnetic sections). The second technique is to require that the photon candidate is "isolated", i.e. only a limited amount of ambient energy, including both electromagnetic and hadronic contributions, is allowed to be present near the photon. In the context of a heavy ion collision, where there is typically a substantial amount of uncorrelated energy present, techniques must be applied to estimate and remove this energy event by event. However, even after doing this, one must account for real photons with an upward fluctuation of ambient energy nearby ("leakage") as well as fake photons with a downward fluctuation, passing the nominal selection criteria. Thus, shower-shape discriminators are typically combined with an isolation requirement, and various means exist to combine this information to estimate the true purity of a photon sample in a data-driven fashion.

The CMS photon measurement is performed using electromagnetic clusters in the CMS ECAL, with the CMS tracks and HCAL used to tag backgrounds from electrons or hadronic decays. The signal from prompt isolated photons is extracted using a two-component template fit to the distribution of $\sigma_{\eta\eta}$, a variable which reflects the width of the cluster in the η direction. The signal is derived from PYTHIA γ+jet events, embedded into real Pb+Pb data events. The background distribution is derived from a set
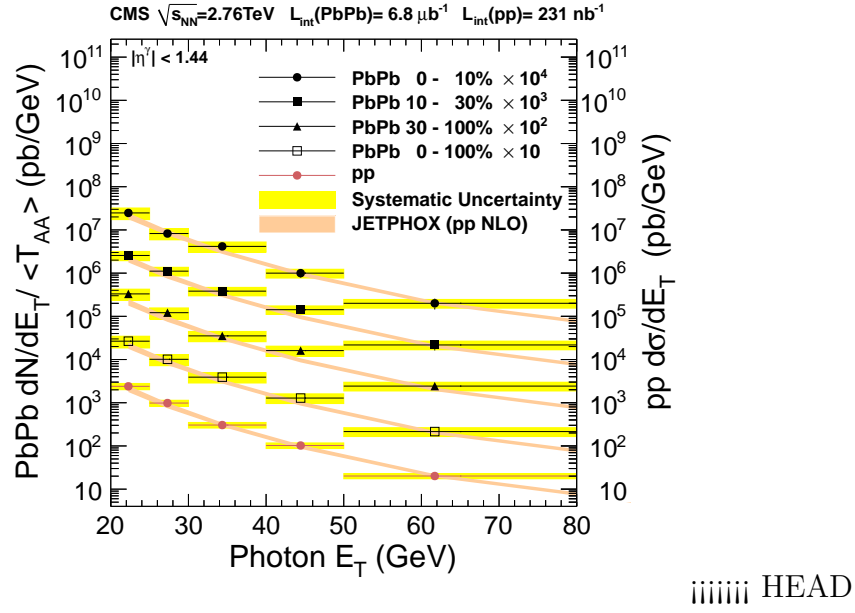
Figure 29: (left) Photon yields scaled by the mean nuclear thickness function for $|\eta| < 1.44$, from CMS data (right) The similar quantity from ATLAS, for $|\eta| < 1.3$, from ATLAS data.
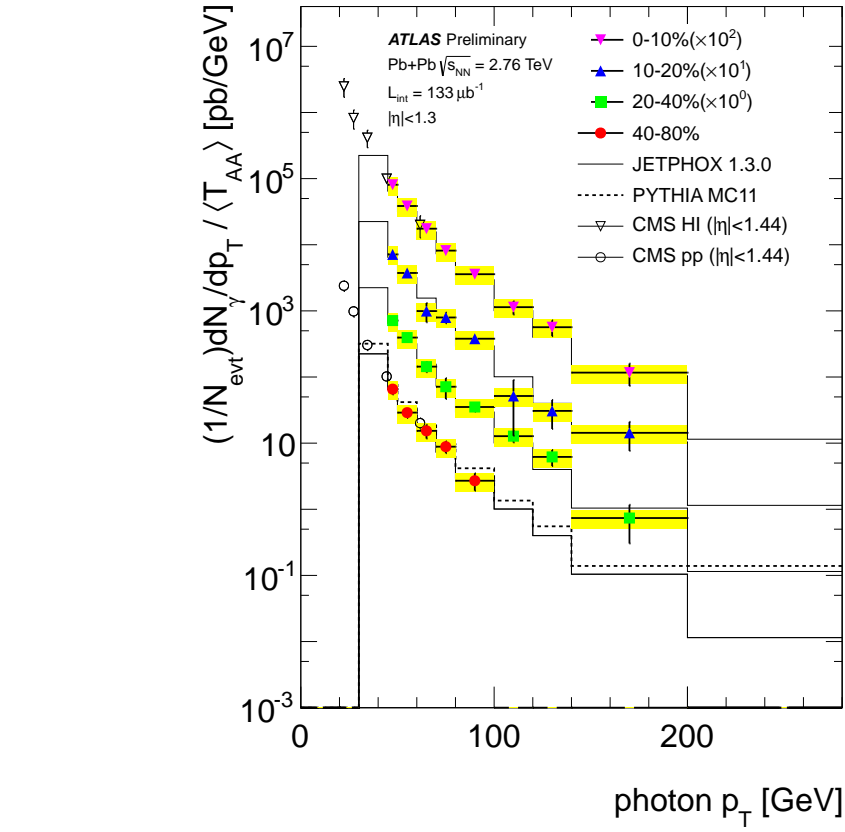

=======

Figure 30: (left) Photon yields scaled by the mean nuclear thickness function for $|\eta| < 1.44$, from CMS data [?] (right) The similar quantity from ATLAS, for $|\eta| < 1.3$, from ATLAS data [?].

¿¿¿¿¿¿¿ acb2b794774419cfb4b81f2c7827a2f97d515634

of photon candidates which are required to fail the isolation selection. After subtracting the extracted backgrounds and correcting for efficiency and resolution effects, the yield of photons is presented as a function of p_T in three centrality intervals as well as a minimum-bias (0-100%) interval. A similar analysis performed on pp data is also shown. In Figure 30(left), both the heavy ion and pp data are compared with an NLO pQCD calculation (using the JETPHOX package) by scaling the calculation by the mean nuclear thickness function $\langle T_{AA} \rangle$ relevant for each interval. It is found that the NLO calculations agree with the pp and heavy ion data in all cases, within the stated statistical and systematic uncertainties. This demonstrates that, like the Z and W results, the photon yields scale with the number of binary collisions. However, while the Z and W results focused on integrated yields, the photons show that there is also no modification of the spectral shape.

ATLAS performed a similar analysis, using the "double sideband" technique to estimate the photon fraction in each p_T and centrality interval for $|\eta| < 1.3$. In Figure 30(right), the preliminary ATLAS data is shown compared with both the CMS data and JETPHOX 1.3.0 results. The ATLAS and CMS data agree well (given the 5% difference in the η range) and ATLAS data agree with JETPHOX out to $p_T = 200$ GeV.

7 Jet quenching

The vastly increased production cross sections for very high p_T hard-scattered jets at the LHC compared to RHIC, combined with the moderate growth of soft particle production forming the "underlying event", opened a new era in studies of jet quenching. The improved signal to background allowed the use of standard reconstruction techniques, calibration methods, background subtraction methods and jet observables developed and well characerized for studies of p+pcollisions. Typically jets in LHC heavy-ion collisions have been reconstructed using the infrared-safe anti-k_t jet clustering algorithm [?] with the radius parameter R varying from $0.2 < R < 0.5$.

Early measurements of hadron production at RHIC clearly showed a large suppression (up to a factor of five to six) in the production rates of high p_T particles in heavy-ion collisions compared to a properly scaled pp reference distribution. [?, ?]. Similarly, the "jet quenching" phenomenon was observed in the suppression of back-to-back hadron production in more central heavy ion collisions [?]. [?, ?]. Yet nearly a decade after the first observation, a detailed understanding of the physics of parton energy loss in the hot and dence medium remained elusive. Reviews of the theoretical state-of-the art before LHC startup can be found in [?, ?].

Compared to hadron-based observables such as those employed at RHIC, measurements of reconstructed jet, dijet and photon-jet final states promise much greater control over the type and kinematics of the initial scattering process and access to information about the energy flow in the evolution of the collision process not otherwise accessible.

7.1 Dijet correlations

The first jet-based observables discussed here are derived from dijet correlations. Within hours after the first heavy-ion collisions at LHC were recorded, it became obvious that there was a large abundance of events were a high p_T reconstructed jet (e.g. $p_T \approx 100\,\text{GeV/c}$) was not accompanied by a back-to-back high p_T partner jet.

In the first study of jets in PbPb collisions at LHC used azimuthal correlations and the momentum asymmetry between the leading and subleading jets to characterize the modification of their properties relative to pp collisions [?]. The jet pairs were selected to have relative azimuthal angle $\Delta\phi = |\phi_1 - \phi_2| >$

$\pi/2$ and their momentum asymmetry was determined as

$$A_J = \frac{E_{T1} - E_{T2}}{E_{T1} + E_{T2}}, \Delta\phi > \frac{\pi}{2}. \tag{6}$$

The leading jet was required to have a transverse energy in the calorimeter of $E_{T1} > 100$ GeV, and the subleading jet was selected to have $E_{T2} > 25$ GeV, after correction for the calorimeter energy response.

In Fig. ?? the dijet asymmetry and $\Delta\phi$ distributions for PbPb data (solid markers) are shown in four bins of ... kground simulat... ns (open circles).
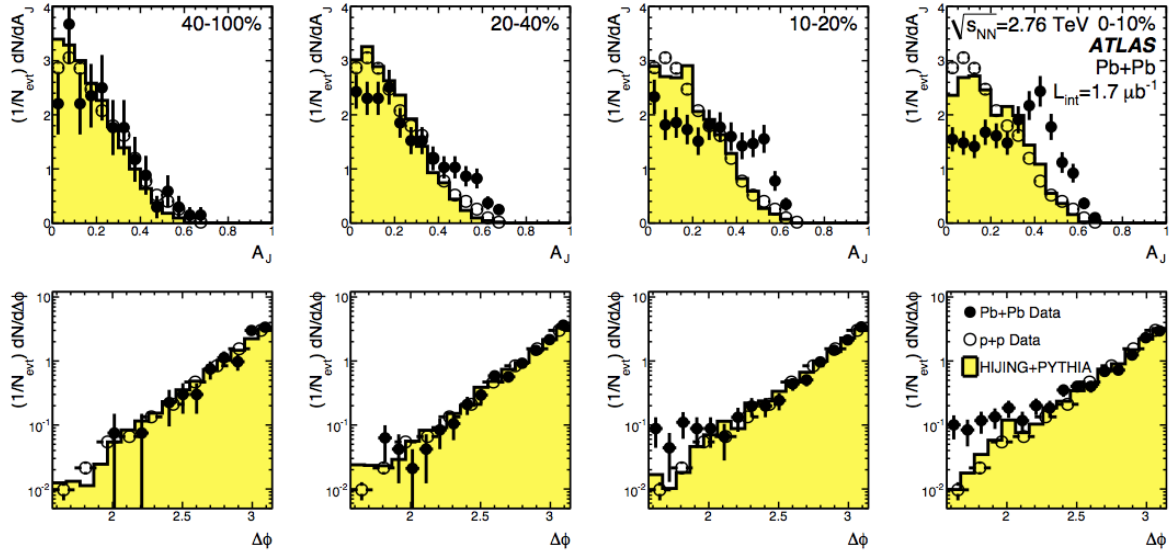

Figure 31: (top) Dijet asymmetry distributions for data (points) and unquenched HIJING with superimposed PYTHIA dijets (solid yellow histograms), as a function of collision centrality (left to right from peripheral to central events). Proton-proton data from $\sqrt{s} = 7$ TeV, analyzed with the same jet selection, is shown as open circles. (bottom) Distribution of $\Delta\phi$, the azimuthal angle between the two jets, for data and HIJING+PYTHIA, also as a function of centrality.

A clear centrality evolution of the dijet asymmetry distribution can be seen, while the azimuthal dijet correlations remain largely unchanged. For peripheral events, the PbPb dijet asymmetry is comparable to that seen in PYTHIA and p+pcollisions. For central events however, the A_J distribution widens significantly, showing a large increase in unbalanced dijet events. The observed trend can be naturally understood in models of parton energy loss in the hot and dense medium, where the back-to-back partons will typically traverse different path lengths, and therefore suffer different amounts of energy loss.

The initial ATLAS and CMS dijet asymmetry analyses were extended using a large dataset of PbPb collisions collected in 2011 by CMS collaboration at $\sqrt{s_{NN}} = 2.76 TeV$. For this analysis, the events were reconstructed using the CMS "particle-flow" algorithm [?, ?], which attempts to identify all stable particles in an event (electrons, muons, photons, charged and neutral hadrons) by combining information from all sub-detector systems. Jets were then reconstructed, after background subtraction, using the anti-k_T sequential recombination algorithm, using the FastJet framework, with radius parameter R = 0.3 [?].

To study the momentum dependence of the amount of energy loss, Fig. 32 presents the dijet asymmetry in bins of leading jet p_T, for 0–20% central events. The distributions show the $p_{T,2}/p_{T,1}$ ratio, instead of A_j, as a more intuitive way of quantifying the dijet momentum asymmetry.

One observes a strong evolution in the shape of the distribution across the various p_T bins, while a significant difference between PbPb data and PYTHYA+HYDJET simulations persists in each p_T bin. The jet momentum dependence of the energy loss can be examined by measuring the dijet asymmetry as
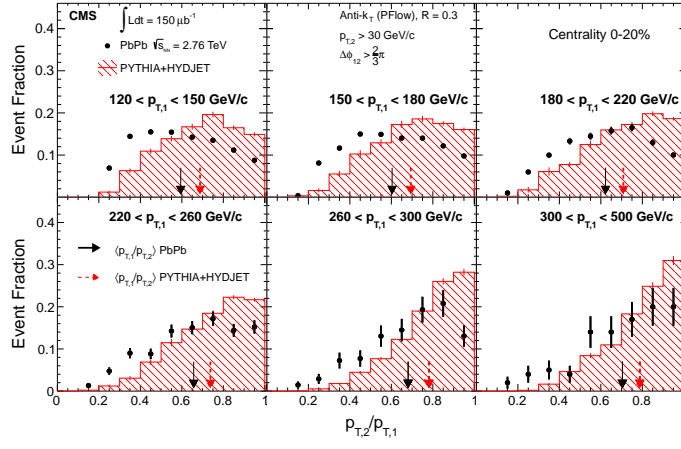
Figure 32: Dijet asymmetry ratio, A_J, in bins of leading jet transverse momentum from $120 < p_{T,1} < 150$ GeV/c to $p_{T,1} > 300$ GeV/c for subleading jets of $p_{T,2} > 30$ GeV/c and $\Delta\phi_{1,2} > 2\pi/3$ between leading and subleading jets. Results for 0–20% central PbPb events are shown as points, while the histogram shows the results for PYTHIA dijets embedded into HYDJET PbPb simulated events. The error bars represent the statistical uncertainties.

a function of leading jet momentum. This was studied by CMS, using $\langle p_{T,2}/p_{T,1}\rangle$. Figure 33 shows the p_T dependence of this ratio for three bins of collision centrality, with PYTHYA+HYDJET simulations shown as squares and PbPb data shown as points.
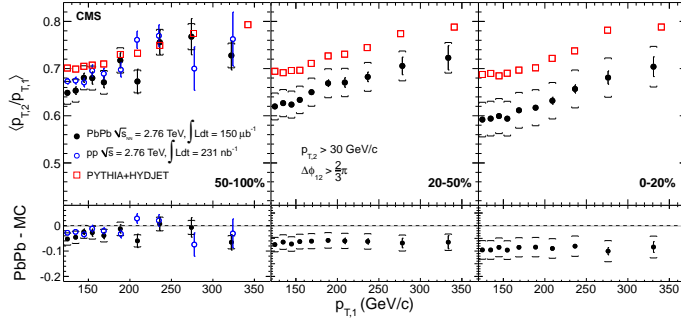

Figure 33: Average dijet momentum ratio $p_{T,2}/p_{T,1}$ as a function of leading jet p_T for three bins of collision centrality, from peripheral to central collisions, corresponding to selections of 50–100%, 30–50% and 0–20% of the total inelastic cross section. Results for PbPb data are shown as points with vertical bars and brackets indicating the statistical and systematic uncertainties, respectively. Results for PYTHIA+HYDJET are shown as squares. In the 50–100% centrality bin, results are also compared with pp data, which is shown as the open circles. The difference between the PbPb measurement and the PYTHIA+HYDJET expectations is shown in the bottom panels.

For all data and simulations, a rising trend of $\langle p_{T,2}/p_{T,1}\rangle$ as a function of leading jet momentum is seen. This is a result of the improving jet energy resolution with increasing jet p_T, and of the evolution in jet kinematics described by the PYTHIA simulations. Importantly, the data show a significantly larger jet asymmetry in central events than in the simulations and in peripheral and p+p data. This effect persists to the highest p_T measured, showing that even the highest p_T jets in PbPb collisions ($p_T > 350$ GeV/c) suffer energy loss as they traverse the medium. A detailed understanding of the energy loss p_T dependence (e.g. fractional vs constant energy loss) will require a full jet MC calculation taking the detector response as a function of p_T into account.

7.2 Suppression of jet yields

A complementary approach to the study of parton energy loss using dijet asymmetry measurements is offered by studies of the nuclear modification factor R_{AA} of jet yields relative to a p+preference or the centrality evolution of R_{CP} relative to peripheral events.

Measurements of the inclusive jet production rates were performed by ATLAS and ALICE. As a result of the path length dependence of parton energy loss in the medium, [?] a reduction in the observed jet yield, normalized per nucleon-nucleon collision, is expected for more central collisions.

In the ATLAS measurement, the jet suppression was quantified using the central-to-peripheral ratio, R_{CP}, comparing jet in a given centrality bin to those in the most peripheral bin, after normalization to N_{coll}.
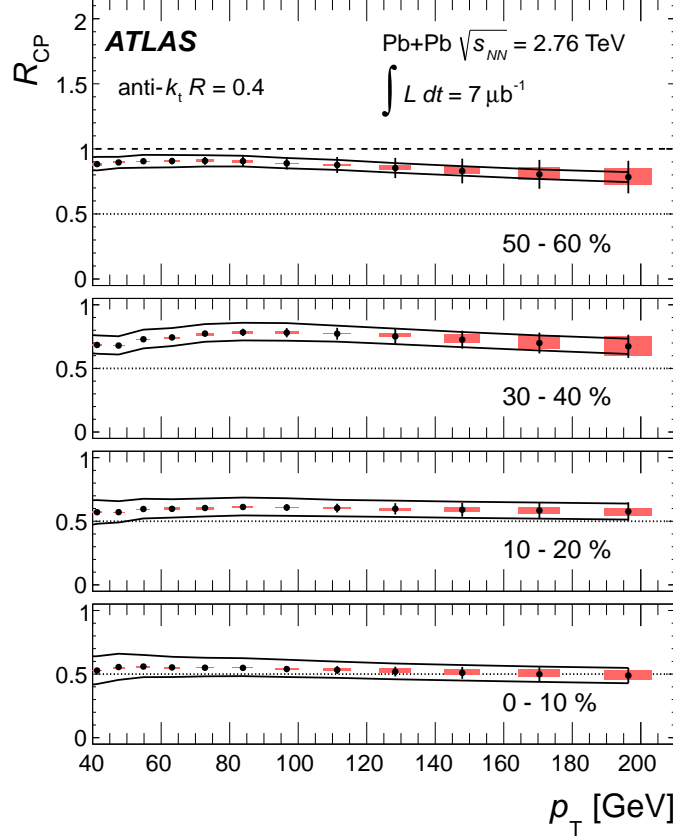

Figure 34: R_{CP} values as a function of jet p_{T} for $R = 0.2$ (left) and $R = 0.4$ (right) anti-k_t jets in four bins of collision centrality. The error bars indicate statistical errors from the unfolding, the shaded boxes indicate unfolding regularization systematic errors that are partially correlated between points. The solid lines indicate systematic errors that are fully correlated between all points. The horizontal width of the systematic error band is chosen for presentation purposes only. Dotted lines indicate $R_{\mathrm{CP}} = 0.5$, and the dashed lines on the top panels indicate $R_{\mathrm{CP}} = 1$.

The resulting R_{CP} values are shown in Figure ?? for $R = 0.4$ jets as a function of jet p_{T} in four bins of collision centrality. Uncertainties are shown as statistical uncertainties, partially correlated systematic uncertainties, and fully correlated uncertainties.

For all centralities only a weak dependence of R_{CP} on jet p_{T} is observed. In contrast, a strong suppression of the jet yield is evident in central collisions, with R_{CP} only reaching a value of about 0.5. This is reminiscent of the value of charged hadron R_{AA} observed by CMS at very high p_{T} which also

reaches a value of about 0.5. The centrality evolution of R_{CP} is consistent with expectations based on the increasing in-medium pathlength traversed by the partons.

Further insight into the pathlenth dependence of parton energy loss may be gained by studying the dependence of the jet yield as a function of azimuthal angle relative to the event plane in peripheral Pb+Pb collisions. This allows the selection of jets traversing different length of the medium at the same medium conditions, whereas the centrality dependence of R_{CP} reflects both the changing pathlength and potential changes in the medium density with centrality.

Related measurements have been performed using the azimuthal dependence of charged hadron yields at intermediate p_T[?, ?, ?, ?, ?]. and very high p_T[?]. For mid-peripheral events, a finite $v_2$for charged hadrons was observed for $p_T$in excess of $40\,\mathrm{GeV/c}$. Compared to these results, jet based measurements offer the advantage of a more direct relationship between observed jet p_T and the energy of the initial parton.
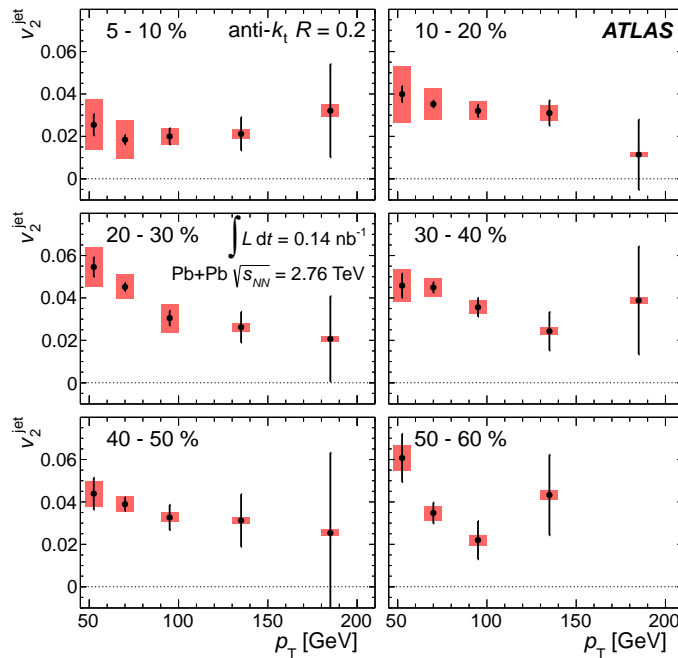

Figure 35: v_2^{jet} as a function of jet p_T in each centrality interval. The error bars on the points indicate statistical uncertainties while the shaded boxes represent the systematic uncertainties (see mbox). The horizontal width of the systematic error band is chosen for presentation purposes only.

The result of the $v_2$measurement for jets reconstructed with the anti-k_T algorithm in $2.76\,\mathrm{TeV}$Pb+Pb collisions is shown in Fig. 35 as a function of jet p_T in bins of collision centrality. A finite value of v_2 is observed for all centrality and p_T, reaching up to 0.05 for mid-central collisions and low jet p_T. The results are in good agreement with those for observed for high p_T charged hadrons [?].

7.3 Modification of jet structure

In addition to the $p_T$and centrality dependence of the suppresion, its dependence on the jet clustering radius parameter is also of great interest, as different energy loss mechanisms may lead to different amounts of energy transport out of the jet cone [?, ?, ?]. This should manifest as a cone-size dependence of the observed jet suppression.

Such a dependence can be seen in Fig.36, which shows shows the ratio of R_{CP} values for $R = 0.3, 0.4$ and 0.5 jets compared to an $R = 0.2$ jets baseline as a function of p_T for central events.
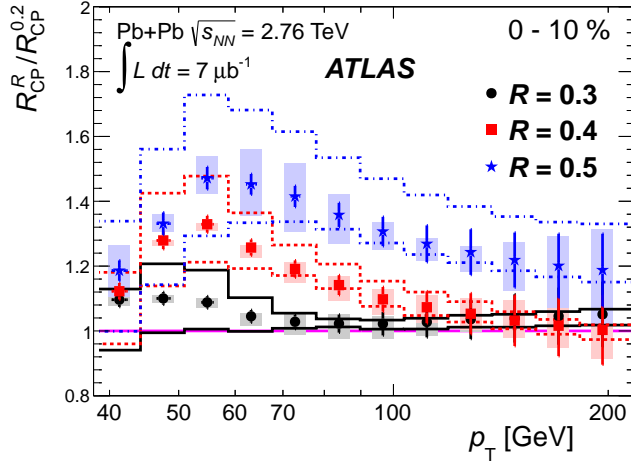
Figure 36: Ratios of R_{CP} values between $R = 0.3, 0.4$ and 0.5 jets and $R = 0.2$ jets as a function of p_T in the 0–10% centrality bin. The error bars show statistical uncertainties (see mbox). The shaded boxes indicate partially correlated systematic errors. The lines indicate systematic errors that are fully correlated between different p_T bins.

The cancellation of various systematic uncertainties allows the observation of a a significant jet radius dependence of R_{CP}, in particular for lower jet p_T. A detailed comparison needs to consider the p_T associated with using different radius parameters to reconstruct the same jets.

Further insight into modifications of the momentum and angular structure of jets in heavy-ion collisions can be gained by measurements of observables used for jet studies in elementary interactions, such as fragmentation functions and jet shapes. Fragmentation functions described the probability for a parton to fragment into hadrons carrying certain fractions of the parton energy. In vacuum, the parton radiation and splitting processes lead to a well-understood characteristic shape of the fragmentation function [**?**].

Figure 37 shows the fragmentation functions for for leading and subleading jets for 0-30% central collisions. Data for Pb+Pb are shown in bins of dijet asymmetry A_J, and compared to a p+p based reference. The lower row of plots shows the ratio of the ratios between the PbPb and pp-based fragmentation functions.

Within the uncertainties of this first measurement, no significant modification of the fragmentation functions in Pb+Pb collisions is observed. This is true even for dijets with large asymmetry, i.e. where the subleading jet has suffered significant energy loss. It is important to note however that only hadrons with $p_T > 4\,\mathrm{GeV/c}$ have been considered in this measurement.

Complementary information about the angular structure of the jets and its modification by the in-medium shower evolution can be obtained by measuring jet shapes, i.e. the jet transverse momentum profile as a function of radial distance to the jet axis [**?**, **?**, **?**, **?**, **?**, **?**, **?**]. The differential jet shape, $\rho(r)$, is defined as

$$ \tag{7} $$

Here r is the radial distance from the jet axis and the transverse momenta of the reconstructed track and jet are p_T^{jet} and p_T^{track}, respectively.

In the CMS measurement of jet shapes, the jet cone is divided into six concentric rings with radial width $\delta r = 0.05$. The transverse momentum profile is determined using the p_T sum for charged particles with $p_T > 1\,\mathrm{GeV/c}$ in each ring, compared to the fraction of the total jet p_T carried by these particles. As for the fragmentation functions, the Pb+Pb jet shapes are compared to a p+p based reference.
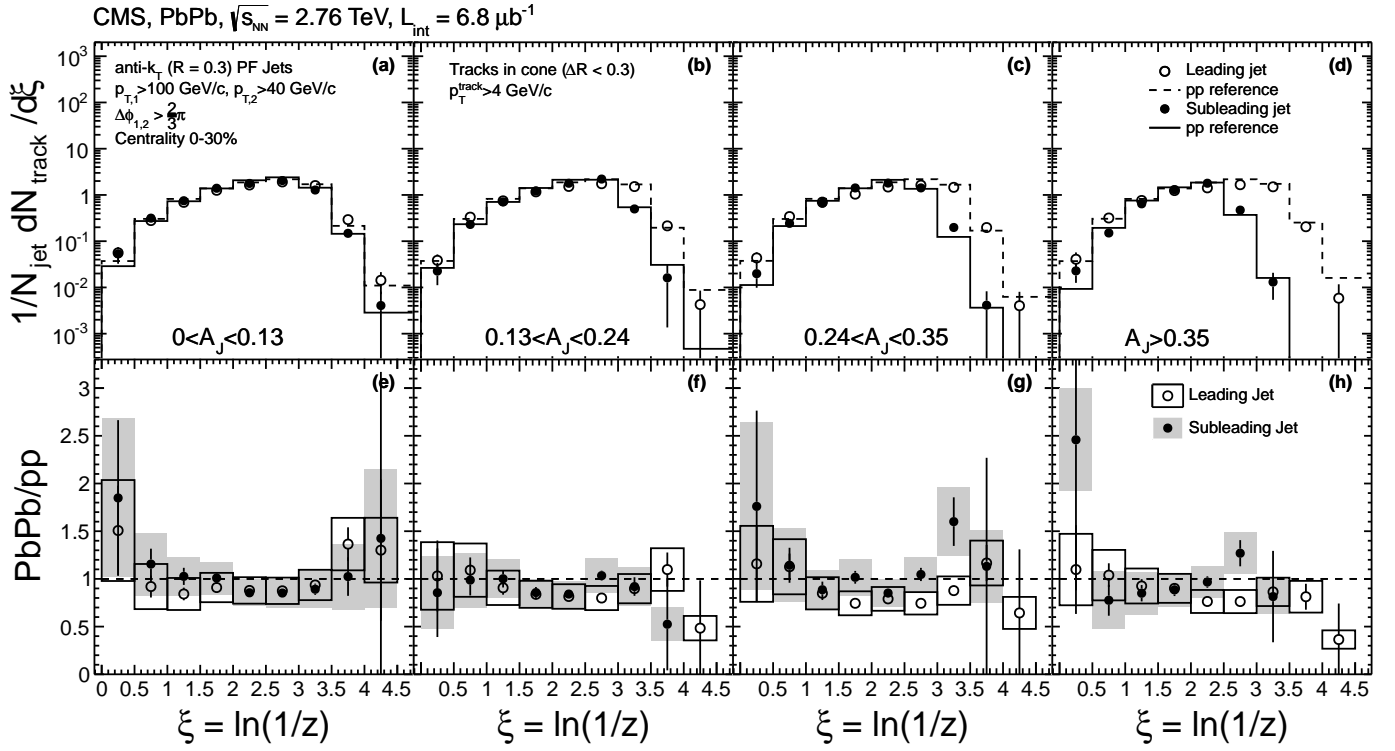
Figure 37: (a–d) Fragmentation functions for the leading (open circles) and subleading (solid points) jets in four regions of A_J in central PbPb collisions compared to the pp reference. (e–h) Ratio of each fragmentation function to its pp-based reference. Error bars shown are statistical. The systematic uncertainty is represented by hollow boxes (leading jet) or gray boxes (subleading jet). (i–l) Jet p_T distributions in PbPb collisions in four regions of A_J (not corrected for efficiency and not unfolded for p_T resolution) compared to the pp-based reference (see mbox). Only statistical uncertainties are shown.

The top row of Fig. 38 shows the differential jet shapes measured in Pb+Pb collisions and the p+p based reference, while the bottom row shows the ratio of the Pb+Pb and p+p distributions. The results are presented in five bins of collision centrality, from most peripheral 70–100% (left) to most central 0–10% (right). For both systems, only a small amount of the total jet energy is carried by particles more than $r > 0.2$ away from the jet axis. However, for central Pb+Pb collisions a large enhancement of the energy fraction at the largest distance to the jet axis ($r = 0.25$-0.3) can be seen. This is qualitatively consisten with the R_{CP} ratios for different jet radii seen by ATLAS, where also an additional part of the jet energy is captured when moving beyond $R = 0.2$, and is in line with the trends predicted in [?, ?], although these calculations were done for a different energy and at parton level, rather than after jet clustering.

7.4 Energy flow in dijet events

The requirements of the background subtraction procedure limit the track-jet correlation study to tracks with $p_T > 1.0$ GeV/c and $\Delta R < 0.8$. Complementary information about the overall momentum balance in the dijet events can be obtained using the projection of missing p_T of reconstructed charged tracks onto the leading jet axis. For each event, this projection was calculated as

$$p_T^{\parallel} = \sum_i -p_T^i \cos\left(\phi_i - \phi_{\text{Leading Jet}}\right), \qquad (8)$$

where the sum is over all tracks with $p_\mathrm{T} > 0.5$ GeV/c and $|\eta| < 2.4$. The results were then averaged over events to obtain $\langle p_\mathrm{T}^{\parallel} \rangle$. No background subtraction was applied, which allows this study to include the $|\eta_{jet}| < 0.8$ and $0.5 < p_\mathrm{T}^\mathrm{Track} < 1.0$ GeV/c regions not accessible for the study in Section **??**. The leading and subleading jets were again required to have $|\eta| < 1.6$.

In Fig. **??**, $\langle p_\mathrm{T}^{\parallel} \rangle$ is shown as a function of A_J for two centrality bins, 30–100% (left) and 0–30% (right). Results for PYTHIA+HYDJET are presented in the top row, while the bottom row shows the results for Pb+Pb data. Using tracks with $|\eta| < 2.4$ and $p_\mathrm{T} > 0.5$ GeV/c, one sees that indeed the momentum balance of the events, shown as solid circles, is recovered within uncertainties, for both centrality ranges and even for events with large observed dijet asymmetry, in both data and simulation.

Further insight into the radial dependence of the momentum balance can be gained by studying $\langle p_\mathrm{T}^{\parallel} \rangle$ separately for tracks inside cones of size $\Delta R = 0.8$ around the leading and subleading jet axes, and for tracks outside of these cones. The results of this study for central events are shown in Fig. **??** for the in-cone balance and out-of-cone balance for MC and data. As the underlying Pb+Pb event in both data and MC is not ϕ-symmetric on an event-by-event basis, the back-to-back requirement was tightened to $\Delta\phi_{1,2} > 5\pi/6$ for this study.

One observes that for both data and MC an in-cone imbalance of $\langle p_\mathrm{T}^{\parallel} \rangle \approx -20$ GeV/c is found for the $A_J > 0.33$ selection. In both cases this is balanced by a corresponding out-of-cone imbalance of $\langle p_\mathrm{T}^{\parallel} \rangle \approx 20$ GeV/c. However, in the Pb+Pb data the out-of-cone contribution is carried almost entirely by tracks with $0.5 < p_\mathrm{T} < 4$ GeV/c whereas in MC more than 50% of the balance is carried by tracks with $p_\mathrm{T} > 4$ GeV/c, with a negligible contribution from $p_\mathrm{T} < 1$ GeV/c.

The PYTHIA+HYDJET results are indicative of semi-hard initial or final-state radiation as the underlying cause for large A_J events in the MC study. This has been confirmed by further studies which showed that in PYTHIA the momentum balance in the transverse plane for events with large A_J can be restored if a third jet with $p_\mathrm{T} > 20$ GeV/c, which is present in more than 90% of these events, is included. This is in contrast to the results for large-A_J Pb+Pb data, which show that a large part of the momentum balance is carried by soft particles ($p_\mathrm{T} < 2$ GeV/c) and radiated at large angles to the jet axes ($\Delta R > 0.8$).

7.5 Photon-jet correlations

In PbPb collisions at the Large Hadron Collider (LHC), the effects of the produced medium have been studied using back-to-back dijets which were observed to be significantly unbalanced in their transverse momenta [**?, ?, ?**]. The advantage of the large yield of dijets (as compared to photon+jet pairs) is, however, offset by a loss of information about the initial properties of the probes, i.e. prior to their interactions with the medium. Correlating two probes that both undergo energy loss also induces a selection bias towards scatterings occurring at, and oriented tangential to, the surface of the medium. At leading order (LO), photons are produced back-to-back with an associated parton (jet) having close to the same transverse momentum. Furthermore, these photons do not strongly interact with the medium. The yields of isolated photons in Pb+Pb collisions were found to match the expectation based on p+p data and the number of nucleon-nucleon collisions, with a modification factor of $R_{AA} = 0.99 \pm 0.31(\mathrm{stat.}) \pm 0.26(\mathrm{syst.})$ [**?**]. Therefore, photon+jet production has been hailed as the "golden channel" to investigate energy loss of partons in the medium [**?, ?**].

"Prompt photons" are photons produced directly in the hard sub-processes. Experimentally, events with enriched production of prompt photons are selected using an isolation requirement, namely that the additional energy in a cone of fixed radius around the direction of the reconstructed photon be less than a specified value [**?**]. This restriction yields "isolated photons" (γ), which consist mostly of prompt photons produced directly in the initial hard scattering. Background photons from the decays of neutral mesons, such as π^0, η, and ω, are suppressed by this isolation requirement, as they are predominantly produced via jet fragmentation. The goal of this analysis is to characterise possible

modifications of jet properties as a function of centrality using isolated-photon+jet events in Pb+Pb collisions. The properties of isolated-photon+jet pairs are studied via the azimuthal angular correlation in $\Delta\phi_{J\gamma} = |\phi^{\mathrm{Jet}} - \phi^\gamma|$ and the transverse momentum ratio given by $x_{J\gamma} = p_{\mathrm{T}}^{\mathrm{Jet}}/p_{\mathrm{T}}^\gamma$. Photons with transverse momentum of $p_{\mathrm{T}}^\gamma > 60\,\mathrm{GeV/c}$ are selected in a pseudorapidity range of $|\eta^\gamma\| < 1.44$, using isolation criteria detailed in Sections **??** and **??**. These photons are then correlated with jets having $p_{\mathrm{T}}^{\mathrm{Jet}} > 30\,\mathrm{GeV/c}$ and $|\eta^{\mathrm{Jet}}| < 1.6$. Parton energy loss due to induced gluon radiation can lead to a shift of the $x_{J\gamma}$ distribution towards lower values. In addition, parton energy loss can cause reconstructed jets to fall below the $p_{\mathrm{T}}^{\mathrm{Jet}} > 30\,\mathrm{GeV/c}$ threshold, leading to a reduction of the fraction of photons with an associated jet.

The asymmetry ratio $x_{J\gamma} = p_{\mathrm{T}}^{\mathrm{Jet}}/p_{\mathrm{T}}^\gamma$ is used to quantify the photon+jet momentum imbalance. In addition to the jet and photon selections used in the $\Delta\phi_{J\gamma}$ study, we further impose a strict $\Delta\phi_{J\gamma} > \frac{7}{8}\pi$ cut to suppress contributions from background jets. Note that photon+jet pairs for which the associated jet falls below the $30\,\mathrm{GeV/c}$ threshold are not included in the $x_{J\gamma}$ calculation. This limits the bulk of the $x_{J\gamma}$ distribution to $x_{J\gamma} > 0.5$. Figure 40 shows the centrality dependence of $x_{J\gamma}$ for Pb+Pbcollisions as well as that for PYTHIA+HYDJET simulation where PYTHIA contains inclusive isolated photon processes. The $\langle x_{J\gamma}\rangle$ obtained from PYTHIA tunes Z2 and D6T agree to better than 1%. Overlaid in the peripheral bin is the $\langle x_{J\gamma}\rangle$ for 2.76 TeV pp data, showing consistency to the MC reference. However the poor statistics of the p+p data and the 50–100% Pb+Pb centrality bin do not offer a strong constraint on a specific MC reference. However, further studies using the 7 TeVhigh statistics p+p data showed a good agreement in $\langle x_{J\gamma}\rangle$ between data and PYTHIA, justifying the use of PYTHIA+HYDJET as an un-modified reference. The dominant source of systematic uncertainty in $\langle x_{J\gamma}\rangle$ is the relative photon+jet energy scale. Its impact on the probability density of $x_{J\gamma}$ is approximately 10% for the intermediate region of $0.6 < x_{J\gamma} < 1.2$. The normalisation to unity causes a point-to-point anticorrelation in the systematic uncertainties, where the upward movement of the probability density at small $x_{J\gamma}$ has to be offset by the corresponding downward movement at large $x_{J\gamma}$. This is represented by the separate open and shaded red systematic uncertainty boxes in Fig. 40. For a given change in the energy scale, all points would move together in the direction of either the open or shaded red box. The N_{part} dependence of the mean value $\langle x_{J\gamma}\rangle$ is shown in Fig. **??**(a).

It is important to keep in mind that the average energy loss of the selected photon+jet pairs does not constitute the full picture. There are genuine photon+jet events which do not contribute to the $\langle x_{J\gamma}\rangle$ distribution because the associated jet falls below the $p_{\mathrm{T}}^{\mathrm{Jet}} > 30\,\mathrm{GeV/c}$ threshold. To quantify this effect, Fig. **??**(b) shows $R_{J\gamma}$, the fraction of isolated photons that have an associated jet passing the analysis selection. The value of $R_{J\gamma}$ is found to decrease, from $R_{J\gamma} = 0.685 \pm 0.008(\mathrm{stat.})$–$0.698 \pm 0.006(\mathrm{stat.})$ for the PYTHIA+HYDJET reference, as well as p+p and peripheral Pb+Pb data, to the significantly lower $R_{J\gamma} = 0.49 \pm 0.03(\mathrm{stat.}) \pm 0.02(\mathrm{syst.})$–$0.54 \pm 0.05(\mathrm{stat.}) \pm 0.02(\mathrm{syst.})$ for the three PbPb bins above 50% centrality.

The first study of isolated-photon+jet correlations in Pb+Pb collisions at $\sqrt{s_{NN}} = 2.76\,\mathrm{TeV}$ has been performed as a function of collision centrality using a dataset corresponding to an integrated luminosity of $150\mu\mathrm{b}^{-1}$. Isolated photons with $p_{\mathrm{T}}^\gamma > 60\,\mathrm{GeV/c}$were correlated with jets with $p_{\mathrm{T}}^{\mathrm{Jet}} > 30\,\mathrm{GeV/c}$to determine the width of the angular correlation function, $\sigma(\Delta\phi_{J\gamma})$, the jet/photon transverse momentum ratio, $x_{J\gamma} = p_{\mathrm{T}}^{\mathrm{Jet}}/p_{\mathrm{T}}^\gamma$, and the fraction of photons with an associated jet, $R_{J\gamma}$. The Pb+Pb data were compared to both p+p data and a PYTHIA+HYDJET MC reference which included the effect of the underlying Pb+Pbevent but no parton energy loss. No angular broadening was observed beyond that seen in the pp data and MC reference at all centralities. The average transverse momentum ratio for the most central events was found to be $\langle x_{J\gamma}\rangle_{0-10\%} = 0.73 \pm 0.02(\mathrm{stat.}) \pm 0.04(\mathrm{syst.})$. This is lower than the value of 0.86 seen in the pp data and predicted by PYTHIA+HYDJET at the same centrality. In addition to the shift in momentum balance, it was found that, in central Pb+Pb data, only a fraction equal to $R_{J\gamma} = 0.49 \pm 0.03\ (\mathrm{stat.}) \pm 0.02\ (\mathrm{syst.})$ of photons are matched with an associated jet at

$\Delta\phi_{J\gamma} > \frac{7}{8}\pi$, compared to a value of 0.69 seen in PYTHIA+HYDJET simulation. Due to the hot and dense medium created in central Pb+Pb collisions, the energy loss of the associated parton causes the corresponding reconstructed jet to fall below the $p_T^{\text{Jet}} > 30\,\text{GeV/c}$ threshold for an additional 20% of the selected photons.

8   Heavy-flavour production

Measurement of charm and beauty production plays a special role in heavy-ion physics: it provides a calibrated probe, as the input p_T spectra are calculable from perturbative QCD and measurable in pp collisions. In addition, this probe is conserved from its production at early stage of the collision until it escapes from interaction region, and is eventually detected. This enables a direct access to its interactions in the QGP, including the low- and intermediate-p_T regime. Two observables are studied:

- transverse momentum dependence of the nuclear modification factor R_{AA} for charm and beauty paricles;

- azimuthal-flow anisotropy of charm and beauty particles, measured as the elliptic-flow coefficient v_2.

These two topics are closely connected: the in-medium heavy-quark energy loss lowers the momenta of heavy quarks, they may then thermalize in the system, and thus participate in the collective-flow dynamics. The simultaneous measurement of the two quantities opens the possibility of the determination of the heavy-flavour transport coefficients.

Two methods are exploited to detect heavy-flavour particles. Reconstruction of invariant mass of exclusive particle decays in a secondary vertex, displaced from the interaction one, is the primary tool. A second method uses the lepton ($\mu^\pm$ or e$^\pm$) p_T spectra to infer the heavy-flavour spectra, presuming that the leptons are produced in semi-leptonic decays of heavy-flavour particles. This way, however, a (p_T-dependent) mixture of charm and beauty is measured. Sometimes a requirement that the lepton is not coming from the interaction vertex is used, which helps to eliminate the background, especially at lower p_T (below 4 GeV). The B-meson production is also accessible with the inclusive decay B $\rightarrow$ J/ψ + X, using J/ψ decays separated from the interaction point.

8.1   Heavy-flavour particle spectra

The p_T spectra of heavy-flavour particles are measured at the LHC in pp and Pb–Pb (and p–Pb) collisions. The pp results are compared to perturbative QCD calculations and other models, giving information about preferred values for parameters, such as renormalization and factorization scales. The charm-particle spectra are measured down to very low p_T (down to 1 GeV in pp) allowing for precise determination of the total charm cross section at LHC energies. The pp spectra also serve as a normalization for Pb–Pb measurements.

In general, the heavy-flavour spectra in heavy-ion collisions are expected to be also suppressed with respect to those in pp interactions, due to the energy quenching of heavy quark when traversing the dense medium. However, the energy loss of heavy quarks is predicted to be different than that of light quarks. For the energy loss by bremsstrahlung radiation, the quark energy loss will be mass dependent. The radiation is suppressed in directions close to that of the quark, for angles below $\Theta_0 \approx m/E = 1/\gamma$, due to a destructive interference (m, E, and γ being the quark mass, energy, and gamma-factor, respectively). The heavier the quark, the larger the exclusion region (i.e. Θ_0, at a given momentum), resulting in smaller energy loss for heavy quarks compared to the light ones. This is the so called dead-cone effect introduced for the vacuum radiation [] and later applied to the medium-induced radiation

in a similar way []. The predicted mass hierarchy is pronounced at p_T comparable with quark masses, and goes progressively away at very high p_T. Recent model calculations include both the radiation and collisional energy loss, which results in larger suppression of heavy quarks, and gets values closer to the expectation for light ones.

There are other effects that modify the expected suppression pattern. At the LHC energies, the light-flavour particles at $p_T \sim \mathcal{O}(10)$ GeV are mostly produced in gluon fragmentation, contrary to heavy-flavour ones produced by fragmentation of the corresponding heavy quarks. Gluons have larger colour charge than quarks by a factor 9/4, consequently a gluon has to suffer more energy loss than a quark. This colour-charge effect is reinforcing the expected difference in suppression between the light- and heavy-flavour particles. Further effects of less importance, taken into account in various models, are nuclear modification of structure functions and harder fragmentation function of heavy quarks compared to the light sector.

Charm mesons are identified in the following decay modes: $D^0 \rightarrow K^-\pi^+$, $D^+ \rightarrow K^-\pi^+\pi^+$, and $D^{*+} \rightarrow D^0\pi^+$ (and their antiparticles), requiring the decay vertex to be displaced from the interaction point. The yields of D mesons are corrected for the feed-down from beauty decays, obtained with model simulations. This contamination amounts to 5–15 % of the yields, depending on p_T and the particle type. The p_T spectra are measured both in pp [] and Pb–Pb [] collisions, and used to construct the nuclear modification factor R_{AA}. The p_T dependencies of R_{AA} for three studied D-mesons are, as expected, compatible. Therefore, the results are combined into an average D-meson R_{AA} according their statistics, dominated by the D^0. Figure 41 compares the average D-meson R_{AA} as a function of p_T in central Pb–Pb collisions, with that of charged particles. The D-meson R_{AA} is perhaps a little bit above the charged-particle one, hinting at less suppression for charm quark, but the difference, if any, is very small. This tendency was recently confirmed with higher statistics charm measurements. The model calculations overlayed on data in Fig. 41 are (I) [**?**, **?**], (II) [**?**], (III) [**?**], (IV) [**?**, **?**], (V) [**?**, **?**], (VI) [**?**], (VII) [**?**], and (VIII) [**?**]. The various models show varying degrees of agreement with the charm results, and in general the inclusion of collisional energy loss improves the description. In model (I) the agreement is obtained by introducing in-medium dissociation of D mesons, in addition to radiative energy loss. The remaining models, which compute also the charge-particle R_{AA}, have not reached good description for both cases, albeit some being not far.

Recently the family of measured D mesons was enlarged with the study of $D_s^+ \rightarrow K^+K^-\pi^+$ decay. As a consequence of strangeness enhancement in heavy-ion collisions discussed in Sec. 3.3, the presence of strange quark may lead to a relative increase of D_s production with respect to other D-mesons. Reported preliminary results show the D_s R_{AA} in p_T region 4–12 GeV above the D-meson R_{AA}, however, still within large uncertainties.

The behaviour of the charm-meson R_{AA} was confirmed by the measurement of the muon spectrum in the forward region $2.5 < y < 4$. The contribution from pion and kaon decays is subtracted from the measured muon spectrum, and the results are presented for $p_T > 4$ GeV, where this background contribution falls below 10 %. The obtained muon p_T spectrum thus represents a mixture of muons from semi-leptonic charm and beauty decays, presumably still dominated by charm at the lowest p_T and progressively becoming beauty dominated for $p_T > 6$ GeV. An analogous analysis of pp data is used for normalization, and the resulting heavy-flavour muon R_{AA} is presented in Fig. 42. The muon p_T, being correlated with the heavy-flavour-particle p_T, is systematically smaller than the latter one (for p_T above a few GeV). Still, the comparison with the D-meson R_{AA} shows qualitative agreement, since the p_T dependence is rather flat. A similar measurement using electrons in mid-rapidity region was also reported [**?**].

In Fig. 42 the preliminary CMS result for R_{AA} from the measurement of non-prompt J/ψ is shown [**?**]. The non-prompt J/ψ particles are selected with careful analysis of the position of the J/ψ-decay point with respect to interaction vertex. These J/ψ's are practically exclusively coming from B-meson decays. Recently reported detailed higher-statistics results on the centrality dependence of the R_{AA} for non-

prompt J/ψ [?] (in p_T range 6.5–30 GeV) in comparison with the ALICE D-meson data (in p_T range 8–16 GeV) demonstrate clearly the larger R_AA for the beauty production than for the charm production, except for peripheral collisions, where the measurements are within their uncertainties. The shift between the p_T ranges takes into account that the J/ψ momentum is lowered in the decay. This is for the first time that, as expected, the energy loss for beauty smaller than that for charm is experimentally observed.

8.2 Heavy-flavour elliptic flow

The primary cause of the elliptic azimuthal asymmetry is the asymmetric collision geometry: in semi-central collisions the overlapping region of the two nuclei has an almond shape, elongated in the direction perpendicular to the event plane (the plane defined by the beam axis and the centres of the colliding nuclei). The elliptic flow of charm was studied by the ALICE collaboration for D mesons using the event-plane method. To estimate the azimuthal position of the event plane, charged tracks detected in the TPC are exploited. Then the yields of different D mesons are measured in the four azimuthal quadrants defined with respect to the event plane. From the yields in the two in-plane and in two out-of-plane quadrants the elliptic-flow coefficient v_2 is calculated. This is done independently for the three mesons: D^0, D^+, and D^{*+}, and, as the v_2 values are compatible, they are then averaged applying beforehand the feed-down correction like in the case of the D-meson R_AA. The v_2 results for the average D meson are presented in Fig. 43 for the centrality in the range 30–50 %. The comparison with the charged-particle v_2 obtained with the same method reveals a similar behaviour: the v_2 values for p_T between 2–8 GeV are compatible. This is the first direct observation of non-zero v_2 for a heavy-flavour particle. The large value of the charm v_2 at p_T around 2 GeV is interpreted as a signature of the in-medium thermalization of charm quarks.

At higher p_T a positive v_2 can be generated by the difference in the in-medium path lengths for charm quarks emitted inside the in-plane azimuthal quadrants compared to those emitted in the out-of-plane quadrants. The shorter path length for the in-plane partons implies less suppression, i.e. larger R_AA for particles produced in this direction, than for those produced in the out-of-plane direction. In fact, the results can be presented as an azimuthally-dependent R_AA, which is equivalent to the azimuthally-integrated R_AA and the v_2. The interpretation of the high-p_T v_2 as a path-length effect opens the possibility of studying the in-medium path-length dependence of the parton energy loss.

The v_2 results for D mesons are complemented by the recently reported elliptic-flow measurements at forward rapidities ($2.5 < y < 4$) for the muons from heavy-flavour decays. They show an effect of similar magnitude. Indication of non-zero heavy-flavour v_2 using the semi-leptonic decays were previously published by RHIC experiments [].
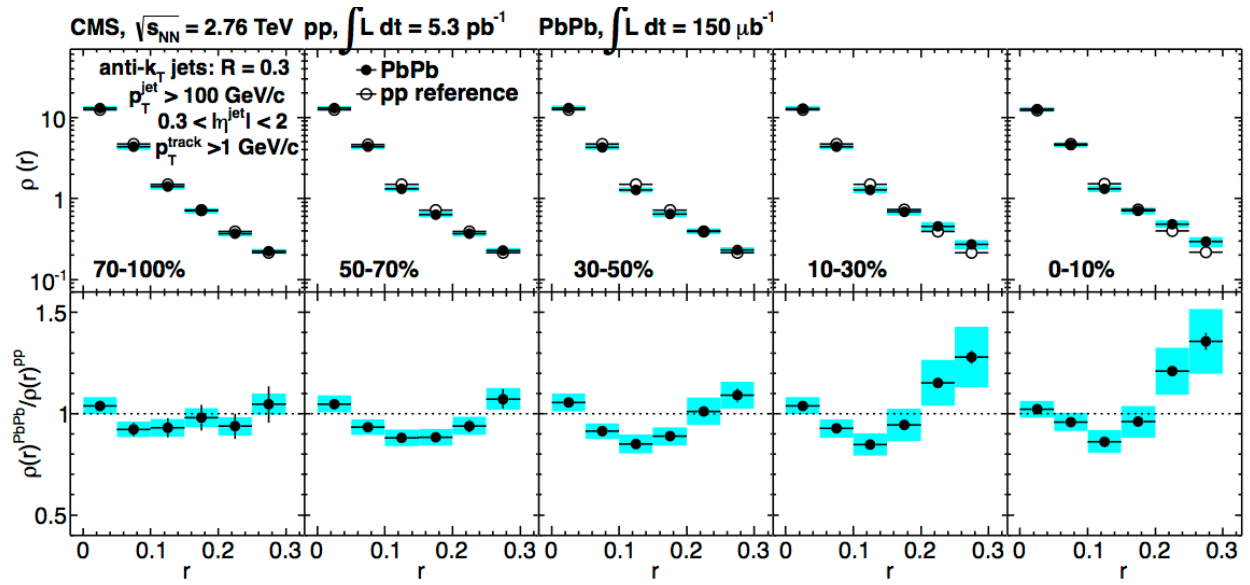
9 Quarkonium production

10 Summary and outlook

Figure 38: (Color online) Top row: Differential jet shapes in Pb+Pbcollisions (filled circles) as a function of distance from the jet axis for inclusive jets with $p_T^{jet} > 100\,\mathrm{GeV/c}$ and $0.3 < |\eta| < 2$ in five Pb+Pbcentrality intervals. The measurements use charged particles with $p_T^{track} > 1\,\mathrm{GeV/c}$. The p+p-based reference shapes are shown with open symbols. The shaded regions represent the systematic uncertainties for the measurement performed in Pb+Pbcollisions, with the statistical uncertainties too
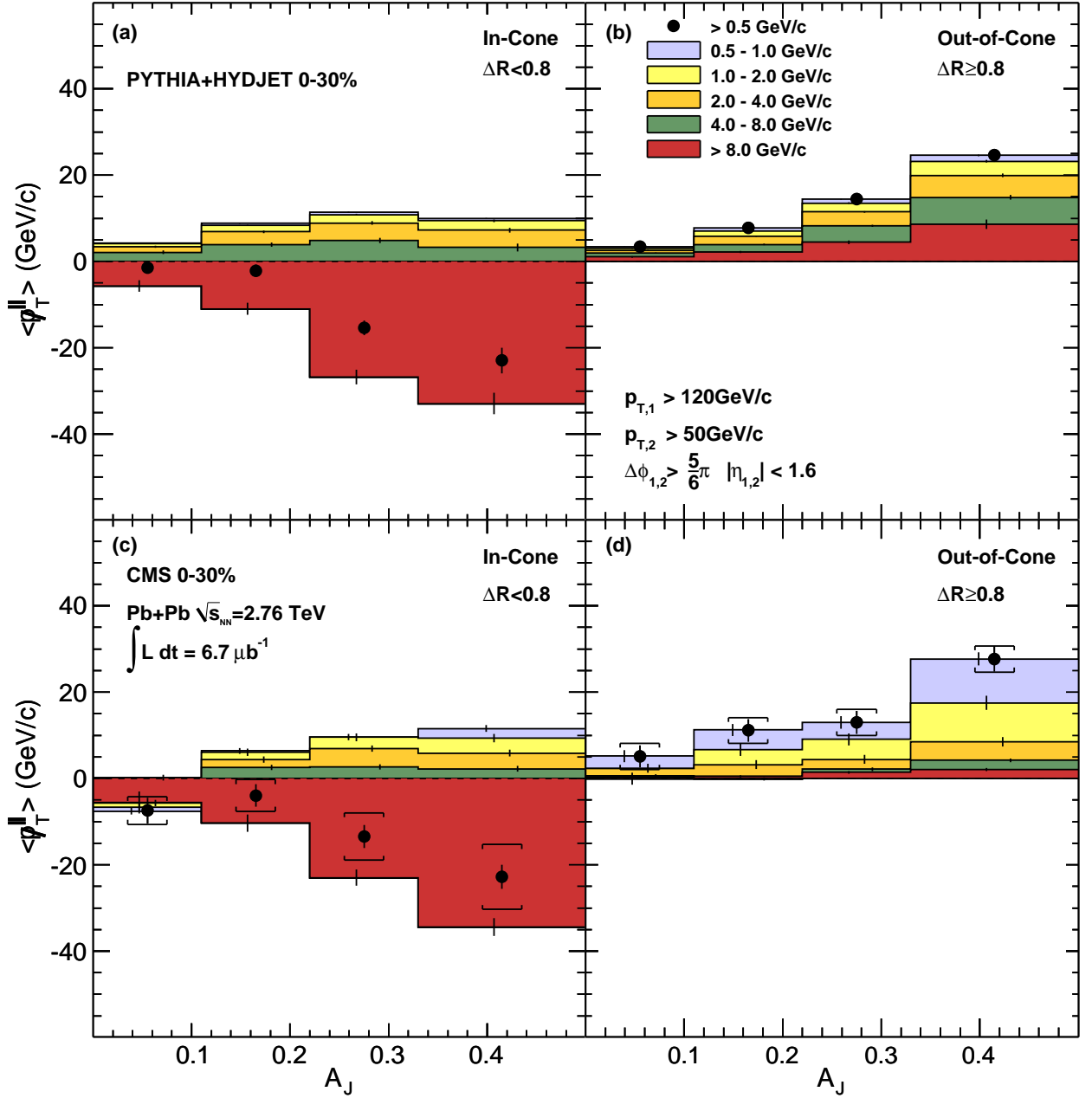
Figure 39: Average missing transverse momentum, $\langle p_{\mathrm{T}}^{\parallel} \rangle$, for tracks with $p_{\mathrm{T}} > 0.5\,\mathrm{GeV/c}$, projected onto the leading jet axis (solid circles). The $\langle p_{\mathrm{T}}^{\parallel} \rangle$ values are shown as a function of dijet asymmetry A_J for 0–30% centrality, inside ($\Delta R < 0.8$) one of the leading or subleading jet cones (left) and outside ($\Delta R > 0.8$) the leading and subleading jet cones (right). For the solid circles, vertical bars and brackets represent the statistical and systematic uncertainties, respectively. For the individual p_{T} ranges, the statistical uncertainties are shown as vertical bars.
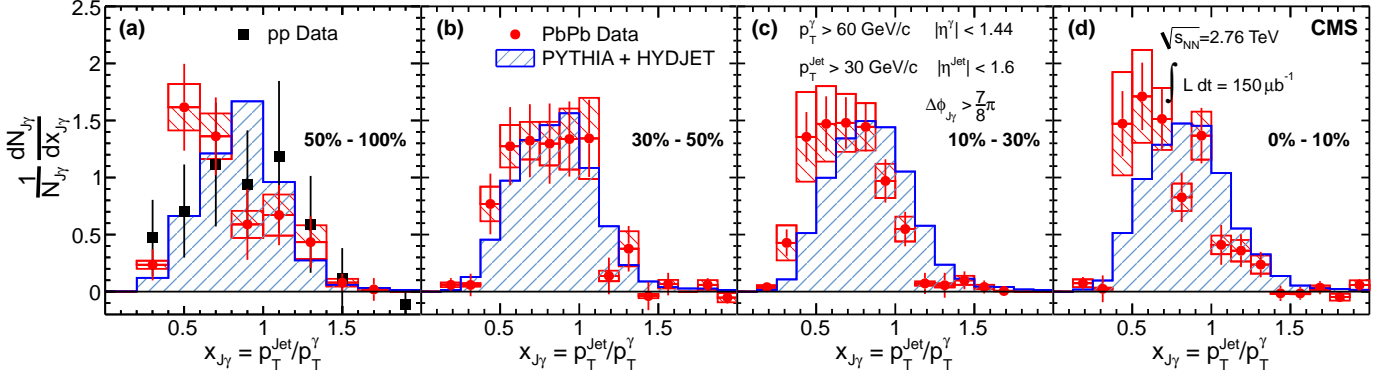
Figure 40: Ratio of p_T between the photon ($p_T^\gamma > 60\,\text{GeV/c}$) and jet ($p_T^{\text{Jet}} > 30\,\text{GeV/c}$, $\Delta\phi_{J\gamma} > \frac{7}{8}\pi$) after subtracting background. The area of each distribution is normalised to unity. All panels show Pb+Pb data (filled circles) compared to p+p data at 2.76 TeV (filled squares), and to the PYTHIA+HYDJET MC simulation (shaded histogram) in bins of increasing centrality left to right. The error bars on the points represent the statistical uncertainty. See mbox for an explanation of the open and shaded red systematic uncertainty boxes.
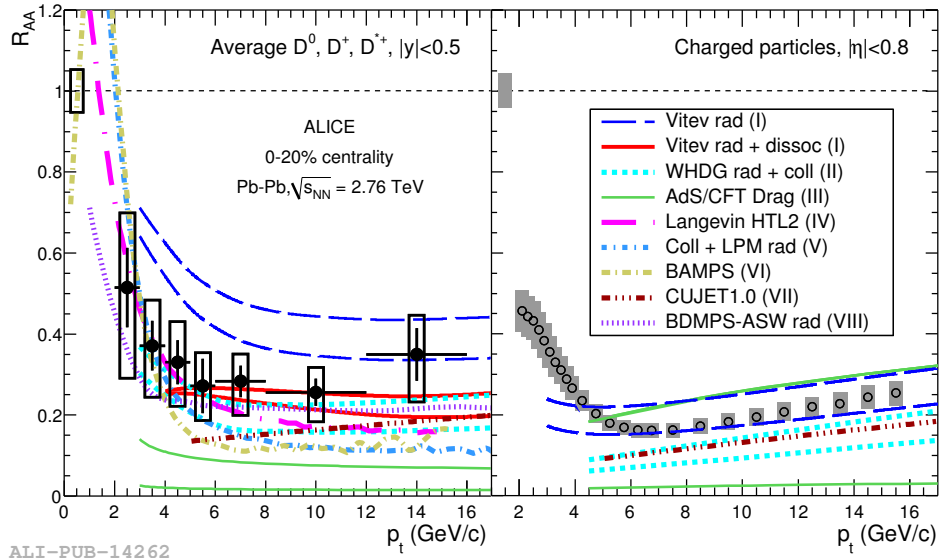

Figure 41: Average D-meson R_{AA} (left) and charged particle R_{AA} (right) as a function of p_T for the centrality between 0–20 %. The normalization uncertainties shown at unity in abscissa are almost fully correlated. The curves represent various model calculations, referred in the text, in some cases depicted as a range. Reproduced from [].
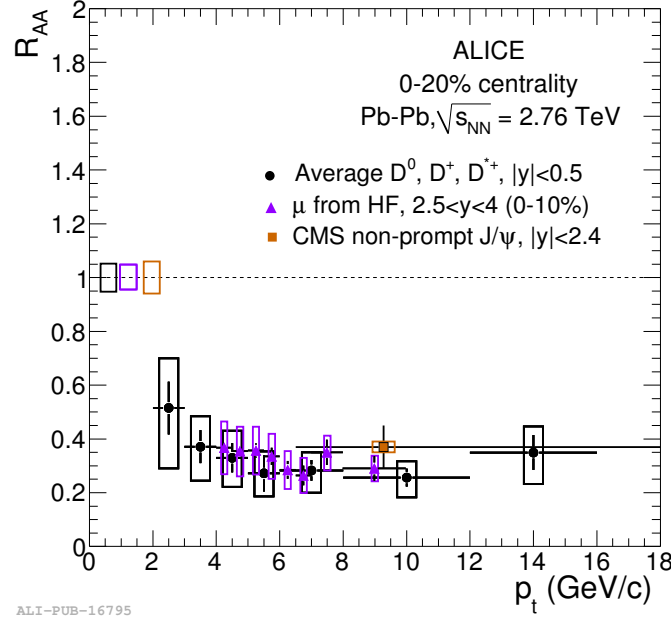
Figure 42: Heavy-flavour muon R_{AA} as a function of p_T compared to the average D-meson R_{AA}. Results are for 0–20 % centrality class of Pb–Pb collisions. CMS preliminary result for beauty R_{AA} from measurement of non-prompt J/ψ is shown with square. Reproduced from [].

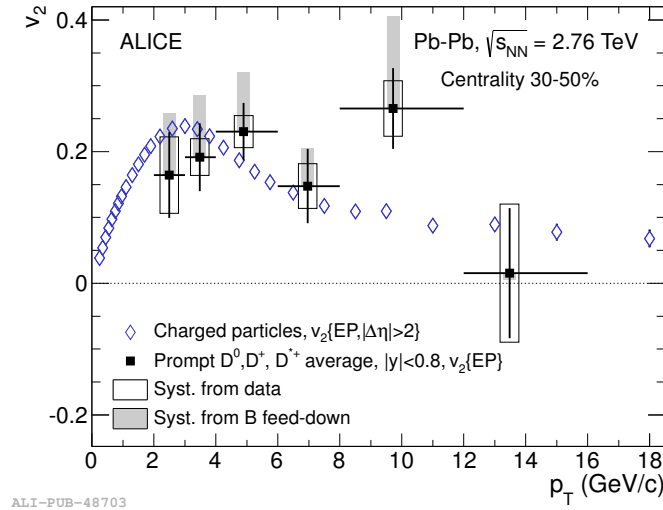

Figure 43: Elliptic-flow coefficient v_2 obtained with the event-plane method, as a function of p_T for the centrality 30–50 %, averaged for D^0, D^+, and D^{*+}, compared to the charged-particle measurement. Reproduced from [].